Supporting Information

Ultrahigh *zT* from strong electron-phonon interaction and low-dimensional Fermi surface

V.K. Ranganayakulu, [‡abc] Te-Hsien Wang,[‡d] Cheng-Lung Chen,[*ef] Angus Huang,[ghi] Ma-Hsuan Ma,[j] Chun-Min Wu,[k] Wei-Han Tsai,[ac] Tsu-Lien Hung,[a] Min-Nan Ou,[a] Horng-Tay Jeng,[*agi] Chih-Hao Lee,[b] Kuei-Hsien Chen,[l] Wen-Hsien Li,[j] Madison K. Brod,[m] G. Jeffrey Snyder,[m] Yang-Yuan Chen,[*an]

[a] Institute of Physics, Academia Sinica, Taipei 11529, Taiwan
[b] Department of Engineering and System Science, National Tsing Hua University, Hsinchu 30013, Taiwan
[c] Taiwan International Graduate Program, Taipei 11529, Taiwan
[d] Department of Physics, National Chung Hsing University, Taichung City 40227, Taiwan
[e] Graduate School of Materials Science, National Yunlin University of Science and Technology, Yunlin 64002, Taiwan
[f] Bachelor Program in Semiconductor Materials and Fabrication, Ming Chi University of Technology, New Taipei City 243303, Taiwan
[g] Department of Physics, National Tsing Hua University, Hsinchu 30013, Taiwan
[h] Center for Theory and Computation, National Tsing Hua University, Hsinchu 30013 Taiwan
[i] Physics Division, National Center for Theoretical Sciences, Taipei 10617, Taiwan
[j] Department of Physics, National Central University, Jhongli 32001, Taiwan
[k] National Synchrotron Radiation Research Center, Hsinchu Science Park, Hsinchu 30076, Taiwan
[l] Institute of Atomic and Molecular Sciences, Academia Sinica, Taipei 10617, Taiwan
[m] Department of Materials Science and Engineering, Northwestern University, Evanston, Illinois 60208, USA
[n] Graduate Institute of Applied Physics, National Chengchi University, Taipei 11605, Taiwan

[‡] These authors contributed equally to this work

Corresponding authors:
* clchen0417@gmail.com (C.L.C.)
* jeng@phys.nthu.edu.tw (H.T.J.)
* cheny2@phys.sinica.edu.tw (Y.Y.C.)

Figure S1 shows the Dresselhaus strategy to promote thermoelectric performance by using quantum-confined structures to engineer qualitatively different behavior of electron density of states (DOS). However, the actual quantum confinement in thin films and nanowires will cause subband splitting, which will reduce the effective band degeneracy impairing the Seebeck coefficient. A better thermoelectric performance would be achieved in bulk, 3-dimensional materials with complex Fermi surfaces as shown in Figure S2. The tube-shaped and double-walled Fermi surfaces, respectively, lead to 2D and 1D DOS without sub-band splitting incurred by quantum confinement.

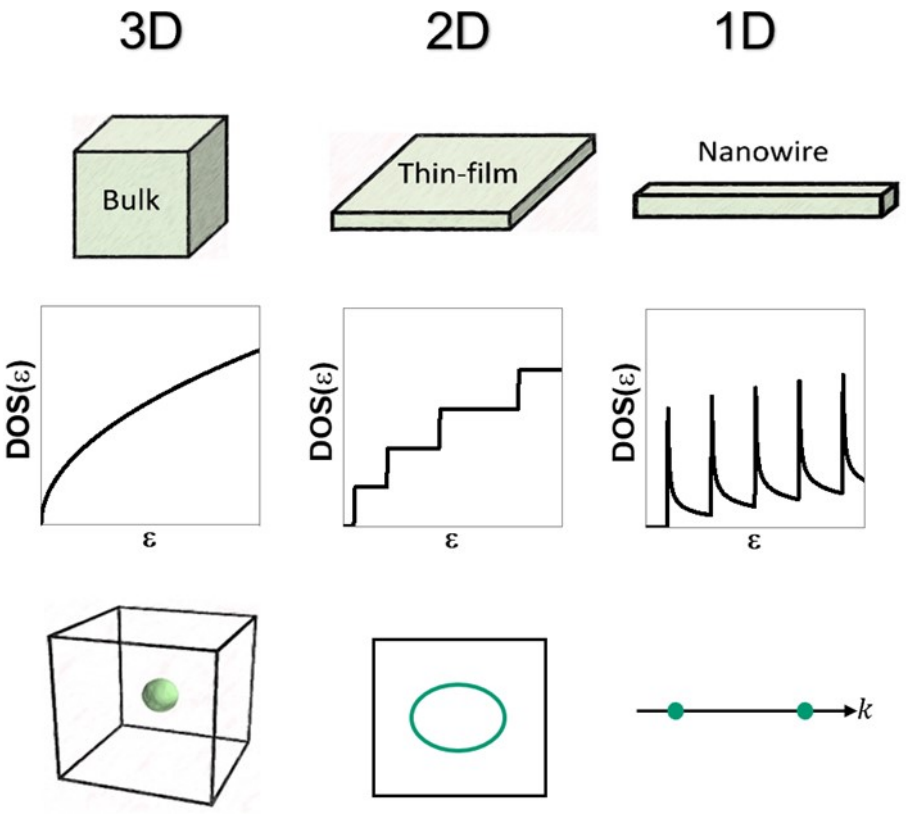

Figure S1 Schematic diagrams of the DOS and Fermi surfaces for quantum confinements of different dimensions.

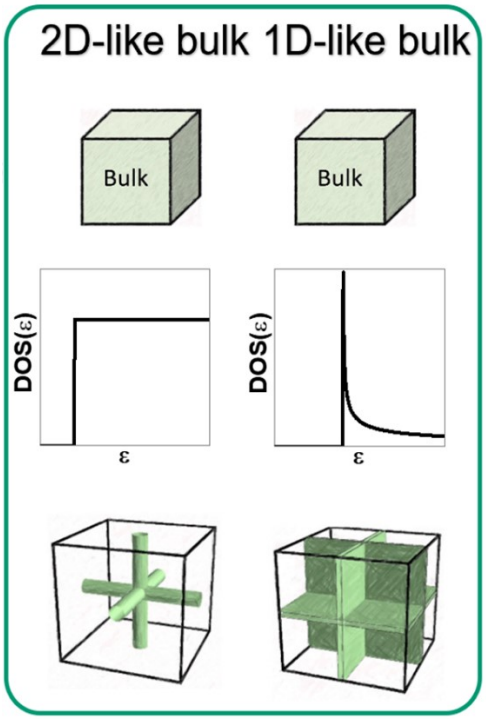

Figure S2 Schematic diagrams of the DOS and Fermi surfaces for low-dimensional electronic structure realized in bulks.

Electronic structure and Fermi surface of C-GeTe

Figure S3 shows the electronic structure of the C-GeTe and the corresponding Fermi surface with the Fermi level slightly lower than the Δ maximum (the red dot in Figure S3c). As can be seen, the Fermi surface looks like a double-walled cube characterizing the 1D-like electronic structure. As shown in Figure S3b, the Γ-F direction, i.e., the crystallographic [110] direction is a nesting vector, while the Γ-L direction, i.e., [100] is not. This would be one of the reasons that the Kohn anomaly cannot be seen in Figure S16.

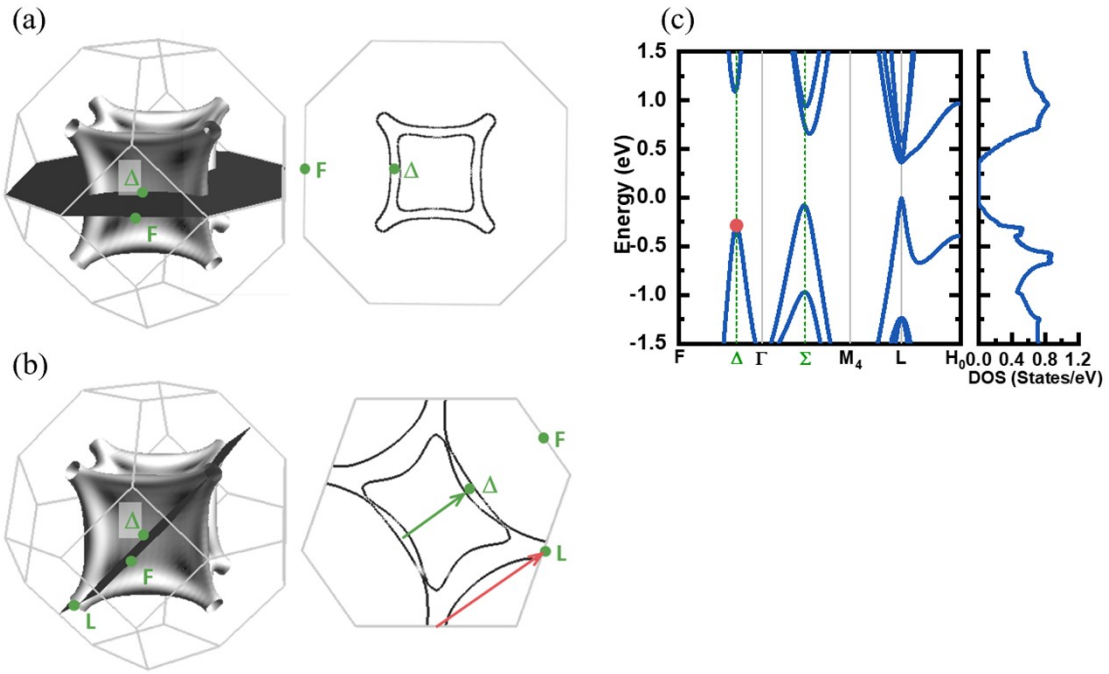

Figure S3 Electronic structure and Fermi surface in C-GeTe. (a, b) Fermi surface and two corresponding cross-sections, in which the Fermi level is slightly lower than the Δ maximum indicated by the red dot in (c). The short green arrow ($\approx 0.35G_0$) and the long red arrow ($\approx 0.5G_0$) indicate the wave vector difference Δk between the initial and final states in the [110] direction (the $\Gamma \rightarrow$F direction). The energy zero is set at the VBM at L point.

Crystal characterizations and microstructures of $(Ge_{1-x-y}Sb_xBi_y)Te$ crystals

A photographic image of a 20 g single-crystalline $(Ge_{0.86}Sb_{0.08}Bi_{0.06})Te$ is shown in Figure S4a. Figure S4b displays its corresponding Laue diffraction pattern of individual planes of a zone axis along [00L]. The *c*-axis of the crystal is approximately 35° offset from the growth direction (Figure S5). It is worth noting that the slight astigmatism of the diffraction spots in Figure S4b suggests that there are short-range ordered defects in the crystal induced by Sb-Bi doping. No impurity phase was shown in diffraction patterns for the pristine and Sb-Bi co-doped GeTe crystals (Figure S4c), confirming the high quality of the single crystals. Figure S4d presents the room

temperature powder XRD patterns of $(Ge_{1-x-y}Sb_xBi_y)Te$ crystals with x = 0, 0.08; y = 0, 0.02, 0.04 and 0.06. All diffraction peaks are indexed to low-temperature rhombohedral phase (*R3m*). Particularly, the peaks of (024) and (220) planes between 2θ = 41°–45° tend to merge into a single peak with increasing Bi/ Sb dopants, signifying the increasing cubic nature of the GeTe structure. Besides, the shift of (202) peak towards lower angles ($2\theta \approx 29.88°$) with increasing Bi content is associated with the size differences between Ge and Bi atoms (Figure S4d). The calculated lattice parameters are summarized in Figure S6a. As Sb-Bi co-doping content increases, the lattice parameters of *a* and *b* increase while the lattice parameter *c* decreases monotonically, this leads the cell volume nearly constant and independent of x and y (Figure S6b). The density of crystals measured by Archimedes method increases from 6.0 g cm^{-3} for pristine GeTe to 6.3 g cm^{-3} for $(Ge_{0.86}Sb_{0.08}Bi_{0.06})Te$ mainly due to the higher atomic weight of Sb and Bi compared to Ge. The angle θ_0 between primitive vectors of the rhombohedral structure at 300 K is getting closer to 60° with increasing doping content, indicating that the Sb-Bi doping makes the crystal structure more cubic-like (Figure S6b). This result is in good agreement with differential scanning calorimetry measurements. The rhombohedral-to-cubic phase transition temperatures (T_c) shifts from 675 K to 600 K with Sb and Sb-Bi doping (Figure S7).

The compositions and the distributions of elements of Ge, Sb, Bi, and Te in $Ge_{0.86}Sb_{0.08}Bi_{0.06}Te$ samples were analyzed using a SEM-EDS, confirming the homogeneous distribution of elements in all measured specimens. From the representative microscale images of energy-dispersive X-ray analysis (EDAX), the homogeneity of constituent elements and the absence of impurities are demonstrated in Figure S8. The bright-field transmission electron microscope (TEM) image of $(Ge_{0.86}Sb_{0.08}Bi_{0.06})Te$ crystal viewed along [110] direction is shown in Figure S4e. Herringbone-like domains containing a high density of streak structures were observed.

These unique streaks are planar defects and similar to the result caused by Sb and Bi single doping in the GSBT crystal lattice.[1] The dark contrast in the image is speculated to be the result of the strain caused by the streak. The high-resolution TEM (HRTEM) image presents the configuration of Ge/Te atoms as shown in (Figure S4f). The inset of Figure S4f is the corresponding selected area electron diffraction (SAED) pattern taken along the zone axis of [110], which can be indexed to the rhombohedral phase (*R3m*). In addition, abundant nanoscale vacancy layers in Figure S4g and stacking fault defects in Figure S4h are evident respectively. Such kind of stacking failures is mainly caused by the abnormal periodic stacking sequence of two-dimensional Bi-Te/ Sb-Te layers in the GeTe crystal. More specifically, these planar defects located in the space are different from the commonly known grain boundary defects and dislocations. It is expected that these diverse structural defects could enhance multiple scatterings of phonons, and contribute to the significant reduction in lattice thermal conductivity. Compared to pristine GeTe, Sb-Bi co-doping in GeTe can create high-density planar vacancies instead of random point defects. The estimated defect concentration of pristine GeTe and $Ge_{0.86}Sb_{0.08}Bi_{0.06}Te$ from HRTEM are 1.1% and 3.5%, respectively (Figure S11). The value of pristine is consistent with the literature report.[2]

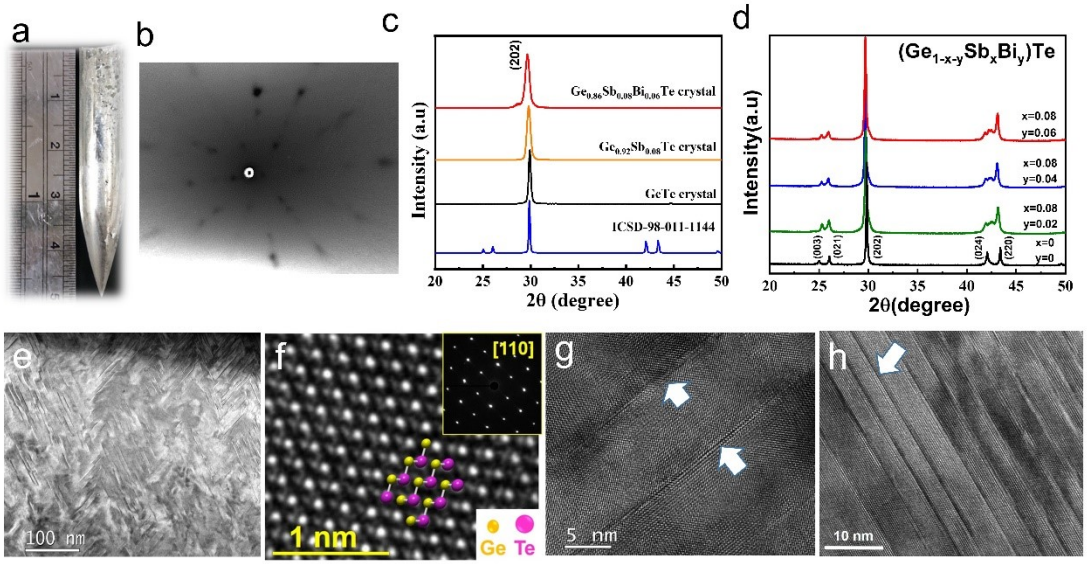

Figure S4 The characterization of $(Ge_{1-x-y}Sb_xBi_y)Te$ (x=0, 0.08; y=0, 0.02, 0.04, 0.06) crystals (GSBT) and electron microscope images of $Ge_{0.86}Sb_{0.08}Bi_{0.06}Te$ crystal. (a) Image of $Ge_{0.86}Sb_{0.08}Bi_{0.06}Te$ single crystal (~5 cm in length and 10 mm in diameter). (b) Laue diffraction pattern of $Ge_{0.86}Sb_{0.08}Bi_{0.06}Te$ crystal along [00L] direction. (c) XRD patterns of $(Ge_{1-x-y}Sb_xBi_y)Te$ crystals. (d) Powder XRD patterns of $(Ge_{1-x-y}Sb_xBi_y)Te$ samples. (e) Low magnification TEM image. (f) Enlarged HRTEM image in a defect-free region along [110] axis, in which Ge and Te atoms are colored in gold and pink (g) HRTEM images of defect layer (mostly Ge vacancy) indicated by white arrows. (h) A number of periodic staking faults (boundaries of two-dimensional Bi-Te/ Sb-Te layers) represented by dark lines, one of which is marked with a white arrow.

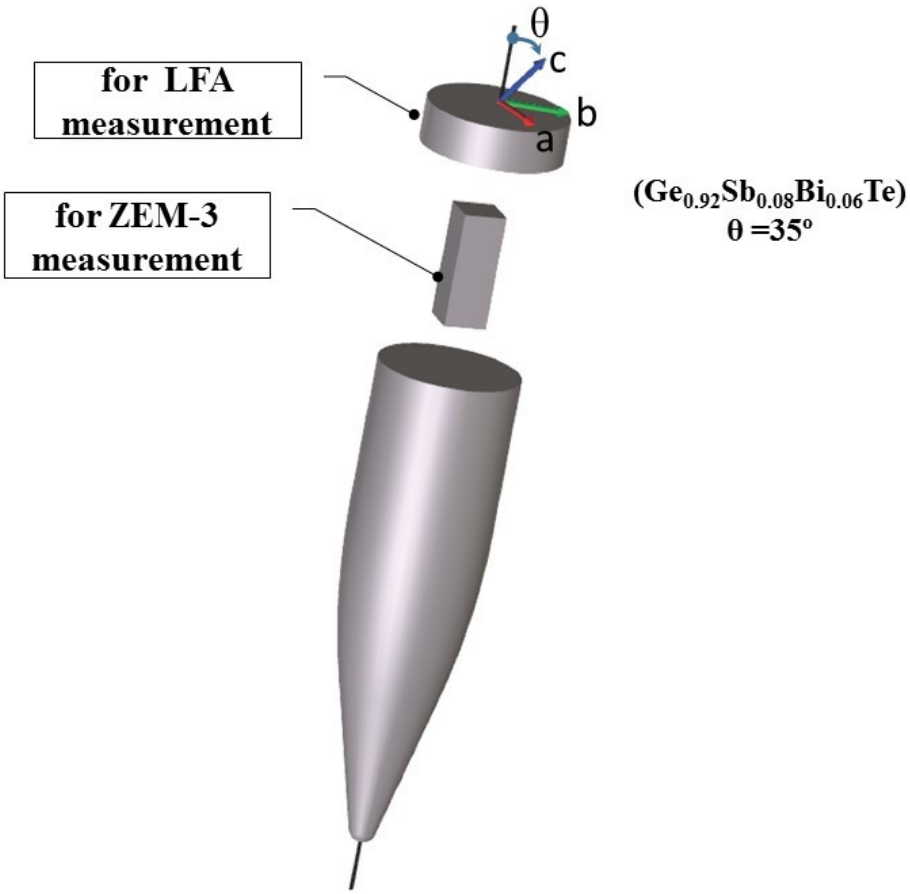

Figure S5 A schematic diagram representing the alignment for the sample used in this study. Figure a, b, c represent crystallographic axes and θ is the tilting angle with respect to the growth direction.

.

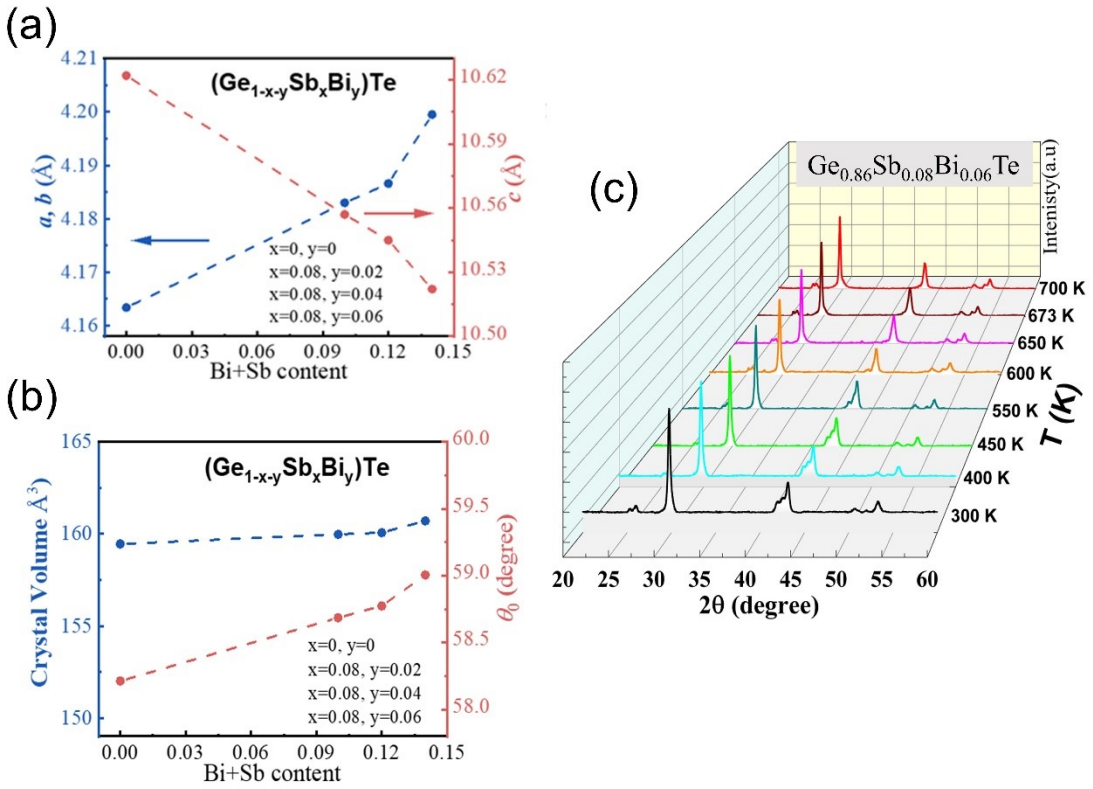

Figure S6 (a) Variation of lattice constants, and (b) cell volume/shape with respect to different doping levels for GeTe and ($Ge_{1-x-y}Sb_xBi_yTe$) crystals at 300 K. The θ_0 is the angle between primitive vectors of the Rhombohedral structure, which becomes the cubic structure if $\theta_0 = 60^\circ$. (c) The structural evolution of $Ge_{0.86}Sb_{0.08}Bi_{0.06}Te$ sample .

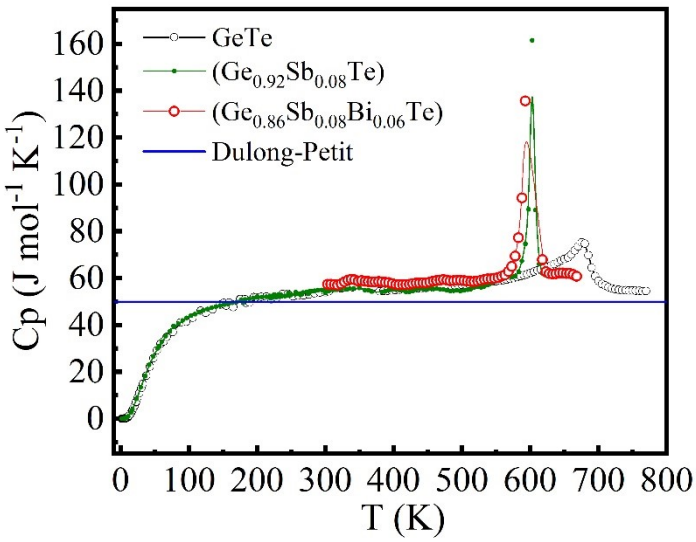

Figure S7 Specific heat of GeTe (48), ($Ge_{0.92}Sb_{0.08}Te$) (48), and ($Ge_{0.86}Sb_{0.08}Bi_{0.06}Te$) as a function of temperature measured using the DSC Q-100. A peak shift in

($Ge_{0.92}Sb_{0.08}Te$) and ($Ge_{0.86}Sb_{0.08}Bi_{0.06}Te$) indicates the shift of T_c towards a lower temperature with Sb- and Sb-Bi doping.

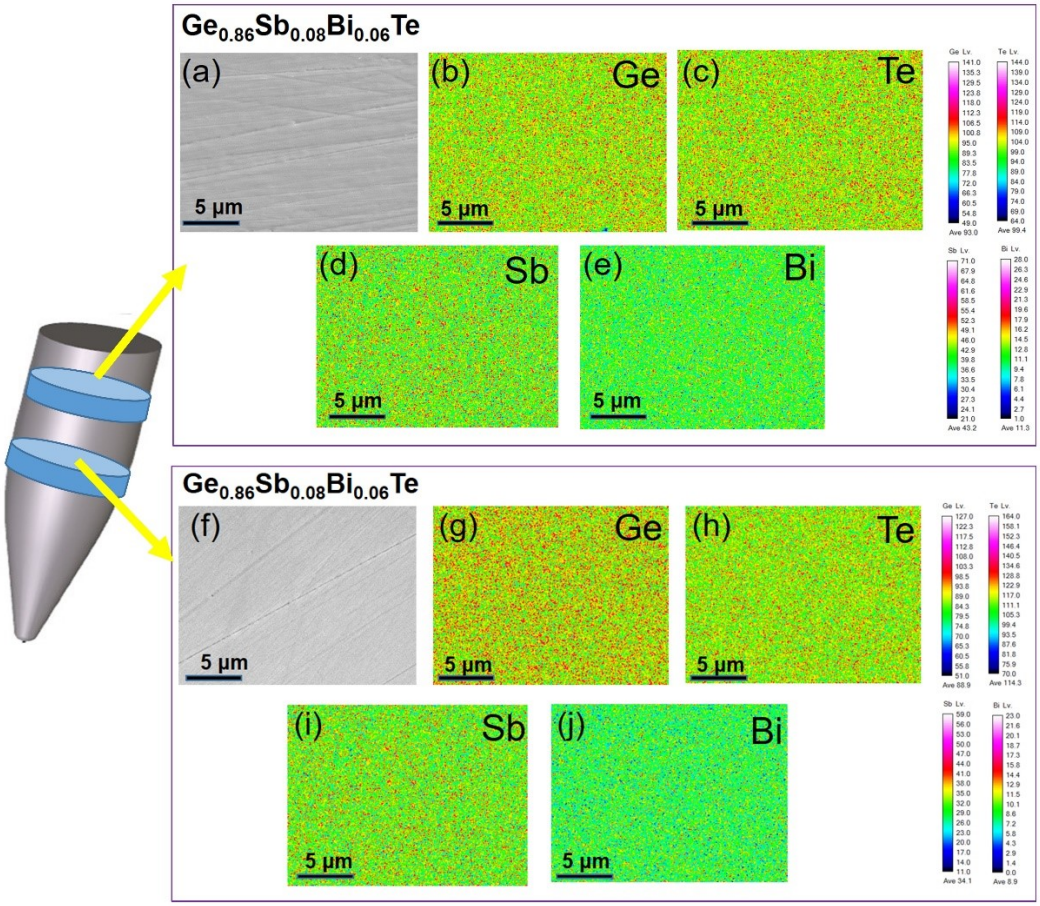

Figure S8 Microstructures and elemental mapping of the $Ge_{0.86}Sb_{0.08}Bi_{0.06}Te$ crystal: (a,f) Secondary electron images, (b,g) Ge mapping results, (c,h) Te mapping results, (d,i) Sb mapping results, and (e,j) Bi mapping results.

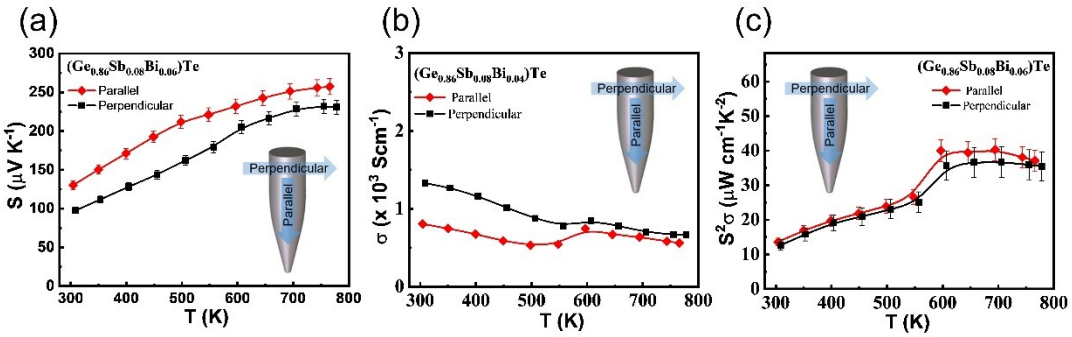

Figure S9 Measurement and comparison of thermoelectric transport properties in different direction of the same single crystal.

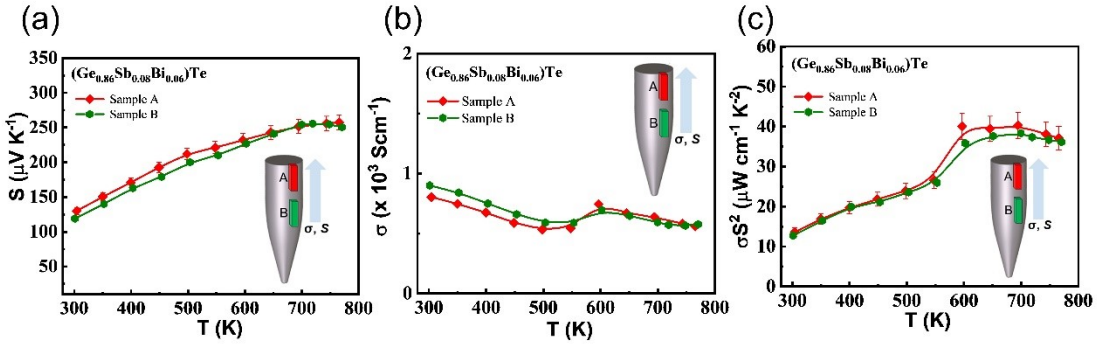

Figure S10 Measurement and comparison of thermoelectric transport properties in different regions of the same single crystal.

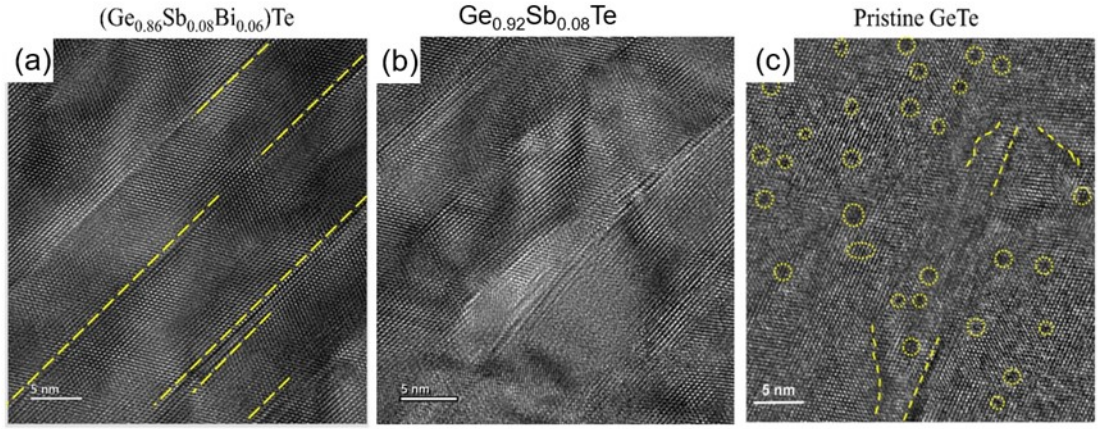

Figure S11 HRTEM images of (a) $Ge_{0.86}Sb_{0.08}Bi_{0.06}Te$ crystal, (b) $Ge_{0.92}Sb_{0.08}Te$, and (c) pristine GeTe. The degree of vacancy ordering in crystals resulting from the single-doping of Sb and Bi is generally more disordered than that in co-doped GeTe but somewhat superior to pristine GeTe. We also simply calculated the defect concentration based on the area occupied by defects in the unit area. The corresponding values of $Ge_{0.86}Sb_{0.08}Bi_{0.06}Te$ and pristine GeTe are 3.5% and 1.1%, respectively.

Valence bands convergence through Sb-Bi codoping

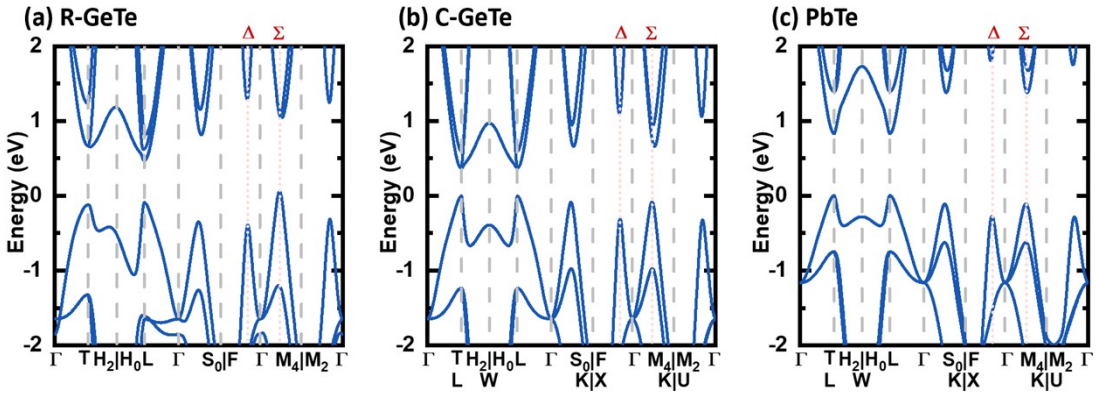

Figure S12 Electronic structures of (a) R-GeTe, (b) C-GeTe, and (c) PbTe. For ease of comparison, the electronic structure of C-GeTe and PbTe are along the same high-symmetry path as R-GeTe even though some k paths in (b,c) are redundant. In (b,c), the second row of the notations of the high-symmetry points is for cubic structure if these notations are different from those in the first row, which are for the rhombohedral phase.

Figures S12a-S12c show the electronic structure of undoped R-GeTe, C-GeTe, and PbTe. As discussed in the main text, the maxima at L (T), Σ, and Δ, are respectively, the representative Fermi levels forming the corners, edges, and surface of the double-walled pyramid bowls of the Fermi surface as shown in Figure 5c. Thus, the energies of the maxima attributed to L (T), Σ, and Δ valleys are listed in Table S1, in which the energy zero is set at the VBM. Unlike the PbTe, whose VBM lies at L, the VBM of the R-GeTe lies at Σ, around which the electronic structure is 2D-like. Thus, the R-GeTe would show higher effective valley degeneracy than the PbTe at low hole concentration. On the other hand, the L maximum for C-GeTe becomes higher than Σ maximum, which is consistent with the results reported by Hong *et al.*[3] The XRD measurement shows that the rhombohedral undoped GeTe becomes more cubic-like with increasing Sb/Bi concentration indicating that the excellent corner (L)-edge (Σ) convergence can be attained by introducing Sb/Bi dopants. Furthermore, as discussed in the main text,

introducing Sb/Bi dopants can increase the electronic energies around the surface of the pyramid bowls including the VBM of the Δ points realizing the simultaneous convergence of the corner, edge, and surface of the electronic structure.

Table S1. Valence band edges of L (T), Σ, and Δ valleys in unit of meV

	R-GeTe	C-GeTe	PbTe
L (T)	-156 (-191)	0	0
Σ	0	-70	-110
Δ	-432	-277	-278

Electronic structures

The electronic structure was calculated through the projector augmented wave (PAW) approach within the framework of density functional theory (DFT) as implemented in the Vienna Ab initio Simulation Package (VASP).[4-6] The exchange-correlation is described in the Perdew−Burke−Ernzerhof (PBE) form of generalized gradient approximation (GGA).[7,8] The spin-orbit coupling is incorporated in the self-consistent calculations, in which the energy convergence threshold was set to 10^{-8} eV. All the internal atomic coordinates and the lattice constant are relaxed until the magnitude of the force acting on all atoms is less than 0.002 eV/Å. The parameters used in the calculations, such as the cutoff of augmented plane waves and sampling of the Brillouin zone, are carefully checked to ensure convergence.

Figure S13 shows the electronic structure for undoped GeTe, single Sb doped structure $Ge_{24}Sb_3Te_{27,}$ and codoped structure $Ge_{24}Sb_2Bi_1e_{27}$. It is well-known that the DFT calculations with standard local density approximation (LDA) or generalized gradient approximation (GGA) generally underestimate the electronic gap.[9] The electronic gap of undoped GeTe obtained by our DFT calculation is 0.3 eV while that

obtained from experiments is 0.6 eV.[10] Thus, the electronic gap in the present study is set to be the measured value of 0.6 eV. Generally, when the energy gap is much larger than the thermal energy $K_B T$ so that the bipolar effect is irrelevant, the TE properties will be insensitive to the magnitude of the energy gap.

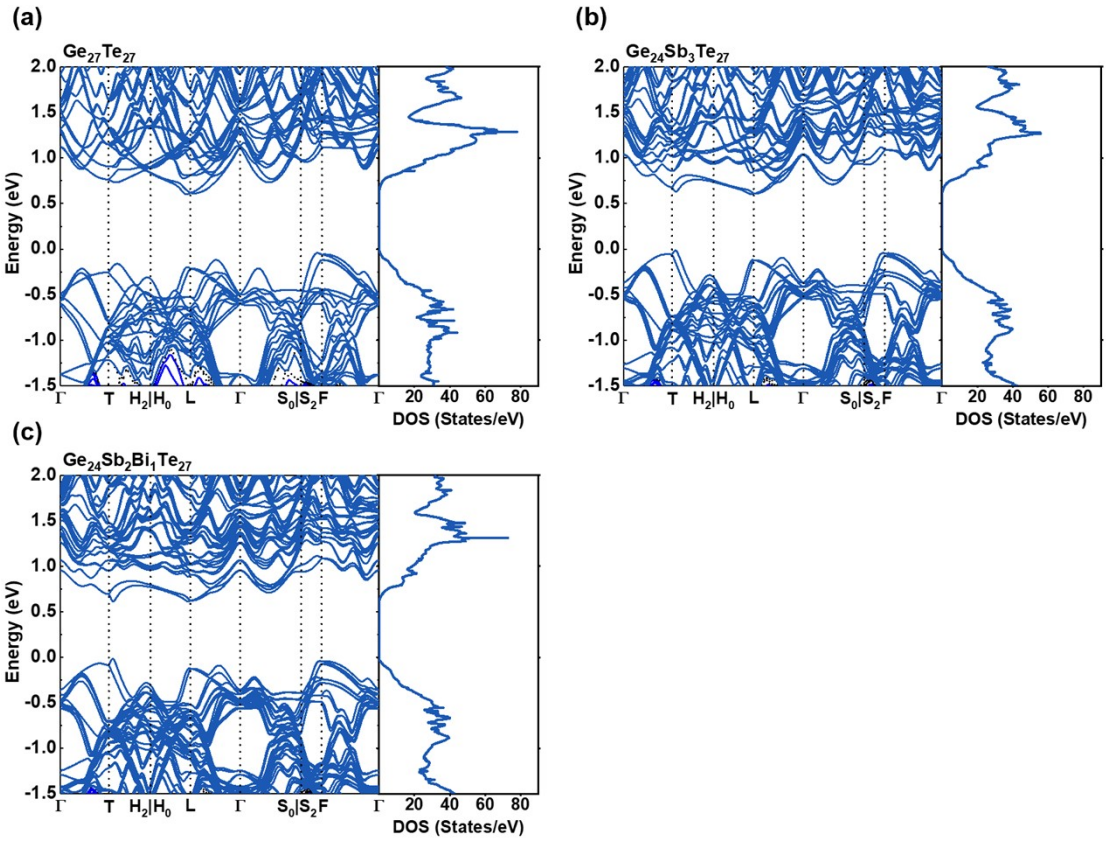

Figure S13 Electronic structure and density of states for undoped structure (a) GeTe (b) single doped structure ($Ge_{24}Sb_3Te_{27}$) and (c) codoped structure ($Ge_{24}Sb_2Bi_1Te_{27}$).

Electronic transport properties

The calculations of Seebeck coefficient S and $R_e = \sigma / \kappa_e R_{WF}$ were carried out with our codes of the Boltzmann transport equation (BTE) based on *ab initio* electronic structure.[11,12] Here the R_e is the ratio of the electrical conductivity σ to the electronic thermal conductivity κ_e divided by the value predicted by the Wiedemann-Franz law,

$R_{WF} = \frac{3e^2}{\pi^2 k_B^2 T}$, and thus is dimensionless. The energy-dependent electronic relaxation time around the Fermi level can be expressed in power-law form as $\tau = \frac{\tau_0 E^{s+0.5}}{D(E)}$.[13] The τ_0 is a constant, and both the S and R_e do not depend on their value. The $D(E)$ is the electronic density of states at energy E obtained from DFT calculations. The characteristic exponent s is given according to the dominant scattering mechanism. It is -0.5 for acoustic phonon scattering, 0 for neutral impurity scattering, and 1.5 for ionized impurity scattering.

Lattice thermal conductivity

The lattice thermal conductivity can be obtained based on our experimental measurement with the help of the BTE calculations described above. In this method, the Fermi level of the specimens is obtained by fitting the measured Seebeck coefficient with that calculated by the BTE, and thus the corresponding R_e of the specimens is known as well. Then, the electronic thermal conductivity, $\kappa_e = \sigma / R_e R_{WF}$, is determined by the measured electrical conductivity σ, and the lattice thermal conductivity, $\kappa_{lat} = \kappa - \kappa_e$, by the measured total thermal conductivity κ.

Dividing κ into κ_{lat} and κ_e assuming different scattering mechanisms

The measured thermal conductivity κ is divided into its electronic part κ_e and its lattice part κ_{lat} based on the measured S and σ, the DFT electronic structure, and BTE calculations as discussed in the previous section. For each material, three similar calculations were performed based on the assumption of different electronic scattering mechanisms including acoustic phonon scattering, neutral impurity scattering, and ionized impurity scattering. As shown in Figures S14 and S15, the resulting κ_{lat} and κ_e obtained based on different scattering mechanisms do not show a significant difference.

For simplicity, the electronic structure of $Ge_{24}Sb_2Bi_1Te_{27}$ is used for all the doped samples.

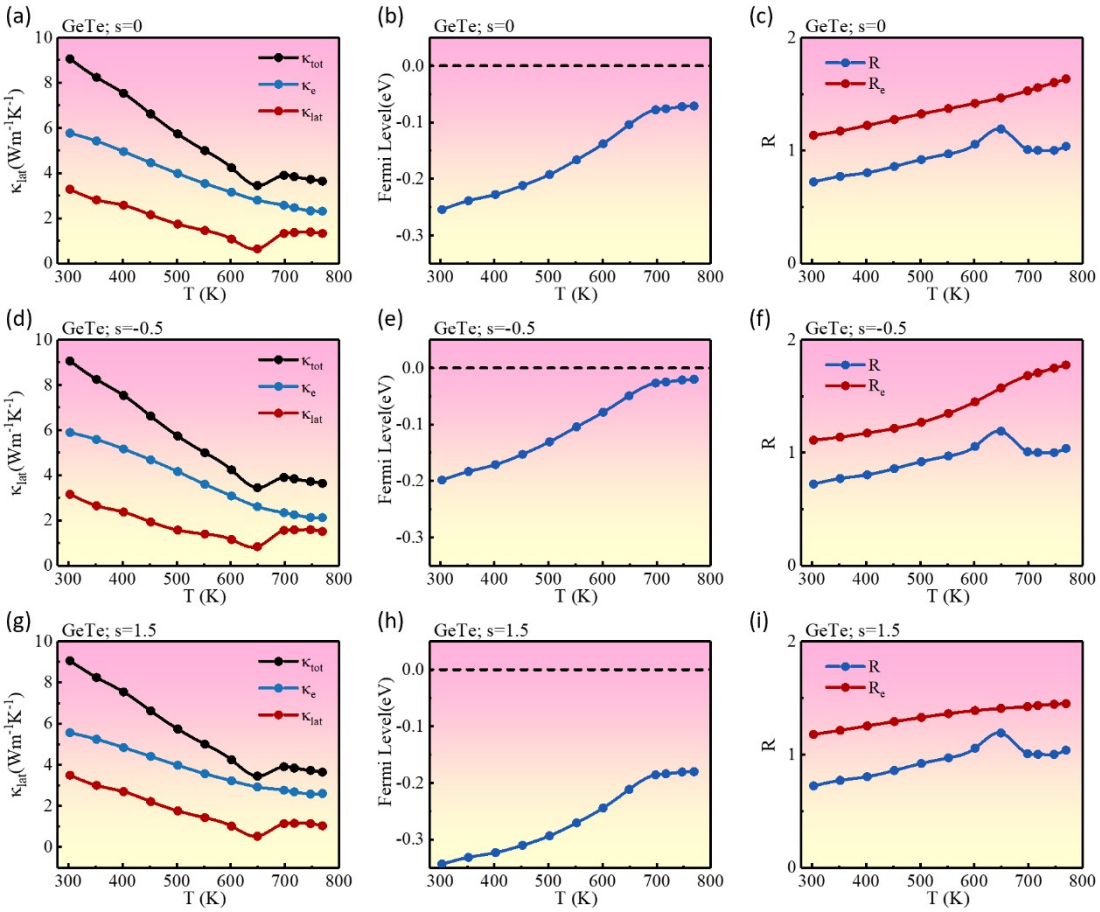

Figure S14 Temperature dependence of thermal conductivity κ and its electronic contribution κ_e and κ_{lat} lattice contribution of undoped GeTe specimens. (a), (d), and (g) are, respectively, obtained under the assumption that neutral impurity scattering (s=0), acoustic phonon scattering (s= -1/2), and ionized impurity scattering (s= 3/2), are dominant scattering mechanisms. (b), (e), and (h) are the corresponding Fermi levels obtained by fitting the measured Seebeck coefficient with that obtained by BTE calculations; (c), (f), and (i) are corresponding dimensionless electrical to (electronic) thermal conductivity ratio $R = \frac{\sigma}{\kappa R_{WF}}$ ($R_e = {}^{\sigma}/_{\kappa_e R_{WF}}$). The κ_e in (a,d,g) is determined by measured σ and then $\kappa_{lat} = \kappa - \kappa_e$ by measured κ.

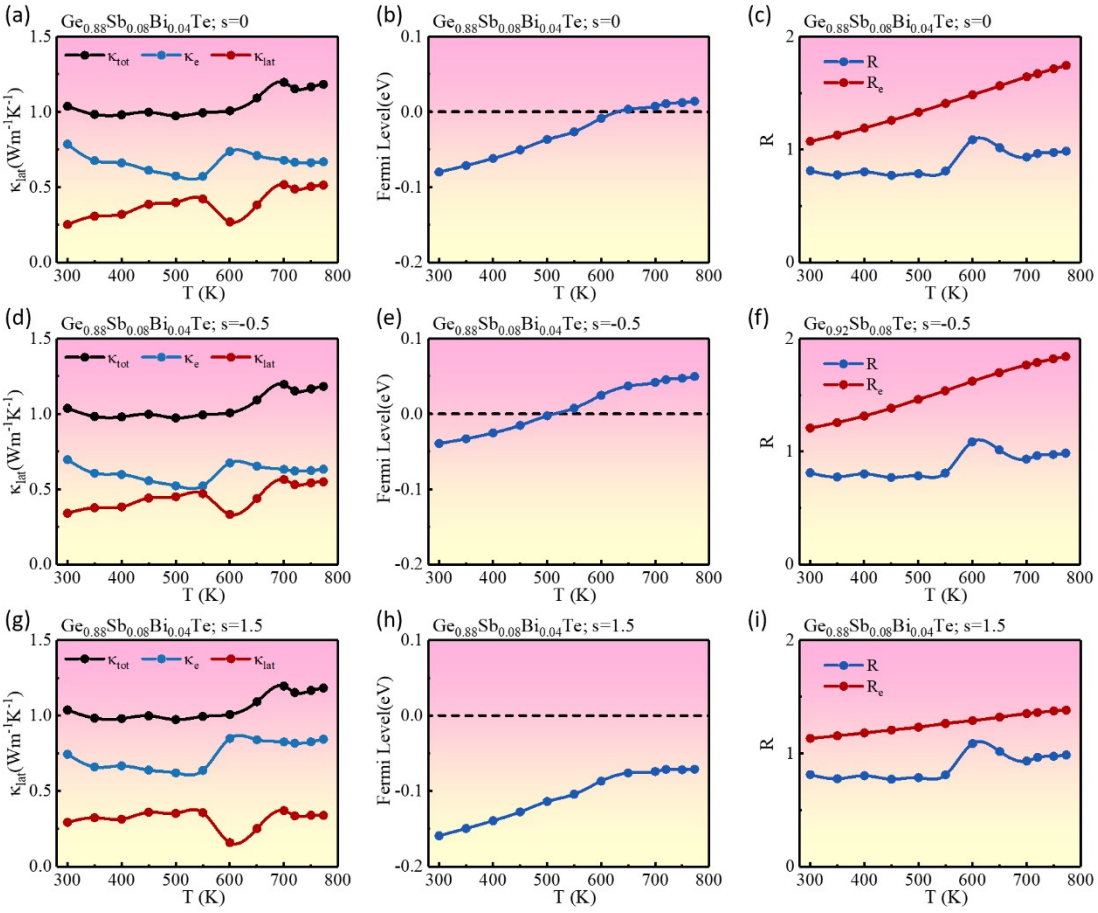

Figure S15 Temperature dependence of thermal conductivity κ and its electronic contribution κ_e and κ_{lat} lattice contribution of $Ge_{0.88}Sb_{0.08}Bi_{0.04}Te$ specimens. (a), (d), and (g) are, respectively, obtained under the assumption that neutral impurity scattering (s=0), acoustic phonon scattering (s= -1/2), and ionized impurity scattering (s= 3/2), are dominant scattering mechanisms. (b), (e), and (h) are the corresponding Fermi levels obtained by fitting the measured Seebeck coefficient with that obtained by BTE calculations; (c), (f), and (i) are corresponding dimensionless electrical to (electronic) thermal conductivity ratio $R = \frac{\sigma}{\kappa R_{WF}}$ ($R_e = {}^{\sigma}/_{K_e R_{WF}}$). The κ_e in (a,d,g) is determined by measured σ and then $\kappa_{lat} = \kappa - \kappa_e$ by measured κ.

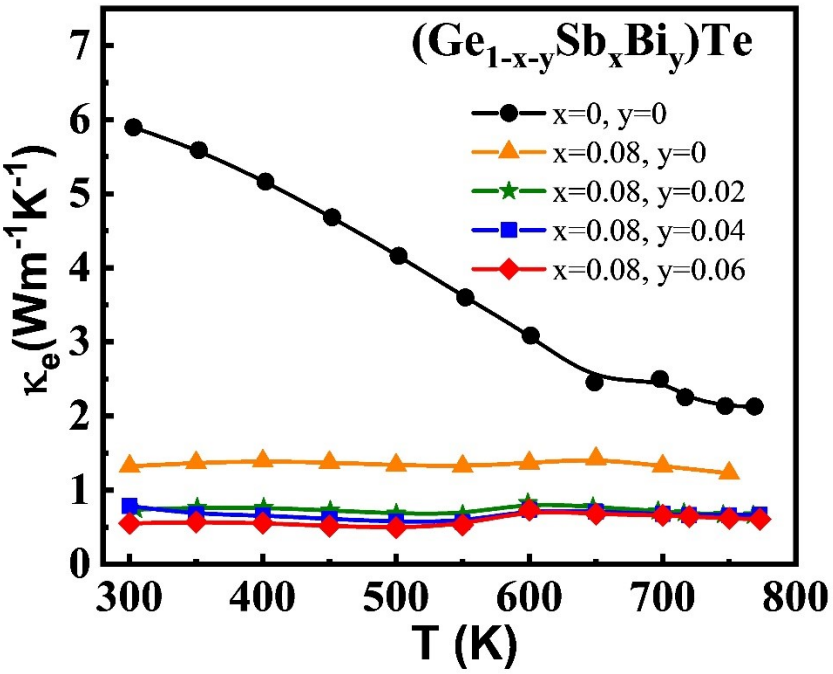

Figure S16 Calculated electronic thermal conductivity for undoped, Sb single doped, and Sb-Bi codoped GeTe crystals.

Phonon dispersion, velocity, and specific heat

To get a statistically representative value of the phonon mean free path l, the phonon velocity v and the specific heat C are required,

$$l = \frac{3\kappa_{lat}}{Cv} \qquad \text{(eq 1)}$$

The sound velocity (i.e., the velocity of acoustic modes around zero energy) should not be reasonable to be representative of the phonon velocity especially for the doped specimens because for doped GeTe, their optical phonon modes are softened with the lowest energy of about 3 meV (Figures S22b and S22c) much lower than thermal energy (26 meV at 300 K) and highly overlapped with the acoustic phonon mode in energy. The acoustic modes of a nearly constant sound velocity should not account for most of the lattice thermal conductivity. Therefore, the ensemble average,

$$v = \frac{\sum_{v} n(E_v) v_v}{\sum_{v} n(E_v)}, \qquad \text{(eq 2)}$$

is used to characterize the phonon velocity. Here v_v and E_v are, respectively, the velocity and the energy of the v_{th} mode, and $n(E)$ the Bose-Einstein distribution function. Figure S17a shows the temperature dependence of the phonon velocity v of undoped, Sb-doped, and Sb-Bi-codoped GeTe specimens. As can be seen, both Sb single doping and the Sb-Bi co-doping can significantly reduce the phonon velocity. Furthermore, with the same amount of dopant concentration, Sb-Bi co-doped GeTe exhibits lower phonon velocity than that of single Sb-doped GeTe, thus having a beneficial effect on the TE performance. As for the specific heat (Figure S17b), Sb/Bi dopant is irrelevant. Above room temperature, all specimens show Dulong-Petit-specific heat of $C \approx 1.5$ J K^{-1}cm^{-3}.

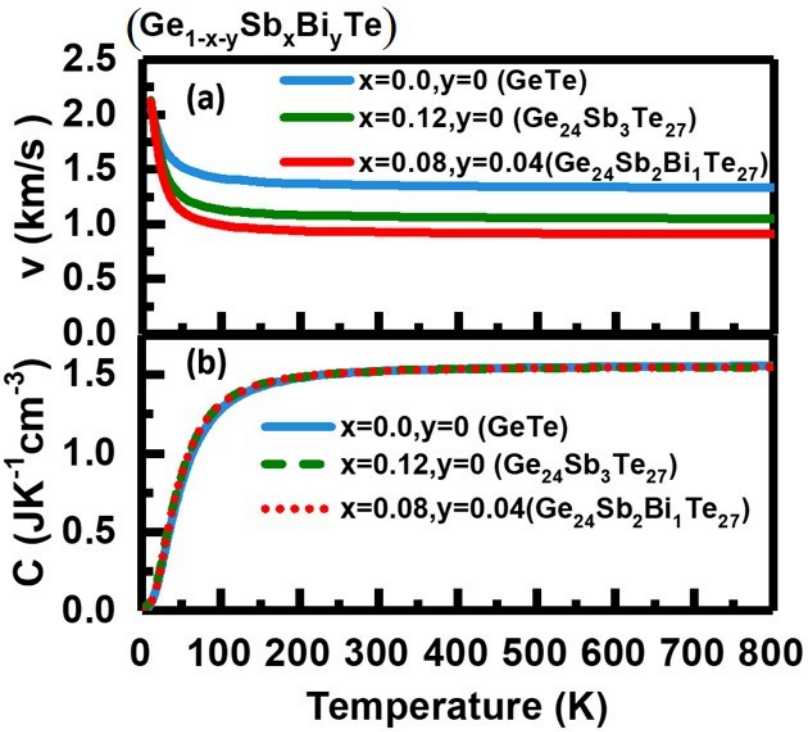

Figure S17 (a) Temperature dependence of the phonon velocity *v,* (b) specific heat *C*.

Statistically representative value of the phonon mean free path

As mentioned previously, the statistically representative value of the phonon mean free path l can be evaluated by eq. 1, in which, for the Sb-Bi co-doped specimens, the lattice thermal conductivity κ_{lat} is about 0.45 $Wm^{-1}K^{-1}$. Above room temperature, both the phonon velocity v and the specific heat C are nearly constant (Figure S17). The phonon velocity is about 900 ms^{-1} and the specific heat is nearly equal to the value given by the Dulong-Petit law of $C \approx 1.5$ $J\ K^{-1}cm^{-3}$. The resulting phonon mean free path l is about 1.0 nm, which is generally much smaller than the distance between the stacking faults/defect layers as presented in Figures S4g, S4h, and S11a indicating that not only the lattice imperfections but also the electron-phonon coupling could be effective phonon scattering sources causing a significant reduction in the lattice thermal conductivity.

It is worth noting that, the resulting representative value of the phonon lifetime (l/v) is 1.1 ps. It is in good agreement with the INS result (0.8-1.7 ps). Furthermore, the lattice thermal conductivity κ_{lat} is extracted from the experiment, which of course incorporates all the scattering mechanisms; the specific heat C and the ensemble average of phonon velocity v are obtained from DFT electronic structure. Thus, even though eq. 1 may look simple, the resulting statistically representative value of the phonon mean free path is probably that determined by the most "realistic" way.

Fitting lattice thermal conductivity using Debye-Callaway model:

Heat-carrying phonons cover a wide range of phonon frequencies, and the corresponding κ_{lat} can usually be analyzed by a modified Debye-Callaway model:[14]

$\kappa_{lat} = \frac{k_B}{2\pi^2 v_s}\left(\frac{k_B T}{\hbar}\right)^3 \int_0^{\theta_D/T} \tau_c x^2 dx$. In the equation, x is $\hbar\omega/k_B T$, ω the phonon frequency, v_s the sound speed, k_B the Boltzmann constant, and ${\tau_C}^{-1}$ the combined phonon relaxation time. Several phonon scattering sources including point defects (PD), Umklapp processes (U), stacking faults (SF), and even electron-phonon scattering (EP) were taken into consideration. According to Matthiessen's rule ${\tau_C}^{-1} = \sum_i {\tau_i}^{-1} = {\tau_{PD}}^{-1} + {\tau_U}^{-1} + {\tau_{SF}}^{-1} + {\tau_{EP}}^{-1} = A\omega^4 + (B_U T e^{-\theta_D/3T} + B_{SF} + B_{EP})\omega^2$. Here, *A* is the point defect scattering parameter, B_U, B_{SF}, and B_{EP} are the scattering parameters for the Umklapp, stacking fault, and electron-phonon scattering processes, respectively. The contributions from Umklapp phonon−phonon scattering (*U*), point-defect scattering (*PD*), stacking fault scattering (*SF*), and electron-phonon scattering (*EP*) were included in the calculation. The relevant reciprocal value of phonon relaxation times is presented by:

Point-defect scattering

$$\tau_{PD}^{-1} = A_S \omega^4 = \frac{V\omega^4}{4v_s^3}\Gamma \quad \text{(eq 3)}$$

Umklapp phonon scattering

$$\tau_U^{-1} = B_U \omega^2 T e^{-\theta_D/3T} \quad \text{(eq4)}$$

Higher order four-phonon scattering[15]

$$\tau_{BH}^{-1} = B_H \omega^2 T^2 \quad \text{(eq5)}$$

Stacking fault scattering

$$\tau_{SF}^{-1} = 0.7\frac{a_{lat}^2 \gamma^2 N_s \omega^2}{v_s} = B_{SF}\omega^2 \quad \text{(eq 6)}$$

Electron-phonon scattering[16]

$$\tau_{EP}^{-1} = B_{EP}\omega^2 \quad \text{(eq 7)}$$

where A is the point defect scattering parameter, B_U, B_H, B_{SF}, *and* B_{EP} are the scattering parameters for the Umklapp (three-phonon), higher-order four-phonon scattering, stacking faults scattering, and electron-phonon scattering processes, respectively. θ_D is the Debye temperature, v_s is average phonon velocity, V is the average atomic volume, Γ is the disorder scattering parameter, N_s is the number of stacking faults per meter, and a_{lat} is the average lattice constant, respectively. The reciprocal sum of phonon relaxation time according to Matthiessen's rule is expressed:

$$\tau_C^{-1} = \sum_i \tau_i^{-1} = \tau_{PD}^{-1} + \tau_U^{-1} + \tau_{BH}^{-1} + \tau_{SF}^{-1} + \tau_{EP}^{-1} \quad \text{(eq 8)}$$

Table S2. Parameters for modeling the κ_{lat}

Parameters	Description	Values
θ_D	Debye temperature	160 K[17]
v_s	Average phonon velocity	1900 m/s[17]
V	Average atomic volume	2.71×10^{-29} m^3
Γ	Point defect scattering parameter	2.18[17]
γ	Gruneisen parameter	fitted
a_{lat}	Average lattice constant	6.02×10^{-10} m
N_s	Number of stacking faults	6×10^6 m^{-1}

Table S3 Fitting parameters are used in Callaway's model

	$A_s\ (s^3)$	$B_U(sK^{-1})$	$B_H(sK^{-2})$	$B_{SF}(s)$	$B_{EP}(s)$
Pristine GeTe	5.03×10^{-42}	8.97×10^{-21}	2.20×10^{-20}	0	0
$Ge_{0.92}Sb_{0.08}Te$	4.00×10^{-41}	1.7×10^{-17}	0	1.11×10^{-15}	0
$Ge_{0.86}Sb_{0.08}Bi_{0.06}Te$	4.00×10^{-41}	1.7×10^{-17}	0	1.11×10^{-15}	5×10^{-15}

Figure S18 shows the lattice thermal conductivity of $Ge_{0.86}Sb_{0.08}Bi_{0.06}Te$, in which only specific scattering processes are considered. From the difference between the blue and green lines (U↔U+PD) or that between grey and purple lines (U+EP+SF↔U+EP+SF +PD), we can conclude that point defect scattering should cause significant reduction in the lattice thermal conductivity. Nevertheless, the dominant scattering process should be the EP as can be seen by comparing the separations of the red line (U+EP) and green line (U+PD) from blue line (U), as indicated by the double headed arrows.

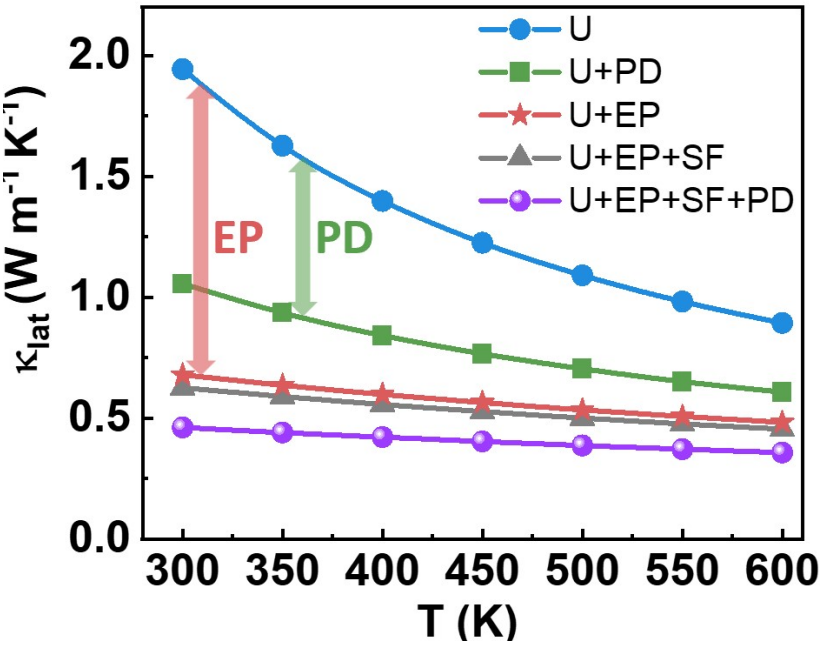

Figure S18 Lattice thermal conductivity of Debye-Callaway model for $Ge_{0.86}Sb_{0.08}Bi_{0.06}Te$. The fitting parameters can be found in Table S3. The purple line indicates that considers all the scattering processes including Umklapp phonon−phonon scattering (U), point-defect scattering (PD), stacking fault scattering (SF), and electron-phonon scattering (EP), while for the other lines only incorporate some of the scattering processes.

Room-temperature Inelastic Neutron Scattering measurement for undoped GeTe along Γ→L direction

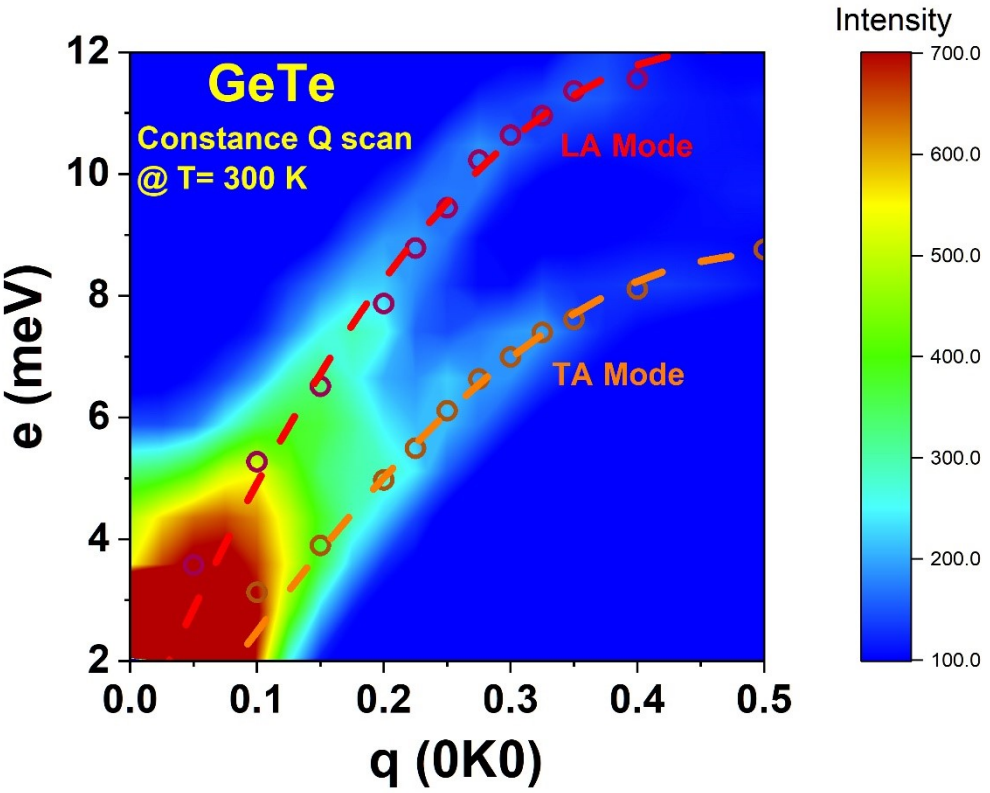

Figure S19 The inelastic neutron scattering for the study of Phonon dispersion on a GeTe crystal, the dashed red and orange lines are guiding lines for LA and TA branches, respectively. The guiding lines are made with the relationship of $E=E_h \sin(q\pi/2)$.

Figure S19 shows the room-temperature phonon dispersion of undoped GeTe measured along [010], i.e., $\Gamma \rightarrow L$ direction. Similar to Figure 4e, the phonon dispersion of undoped GeTe measured in [110], i.e., $\Gamma \rightarrow F$ direction, it does not show clear Kohn anomaly while the Kohn anomaly is clearly observed in Sb-Bi codoped GeTe at both 300 and 610 K (see Figures 4b and 4f). Two reasons would cause the absence of Konhn anomaly in Figure S19. First, as discussed in the main text, the absence of Sb-Bi doping results in lower energy of Δ valley than that of Sb-Bi codoped specimens. Thus, the

undoped GeTe needs more hole concentration to form a 1D-like electronic structure. Second, as shown in Figure S3b, the $\Gamma \rightarrow F$ direction is along the nesting vectors while the $\Gamma \rightarrow L$ does not. As a result, the Kohn anomaly cannot be seen in the undoped GeTe by the INS measurement along the $\Gamma \rightarrow L$ direction.

Crystal structures in the calculations

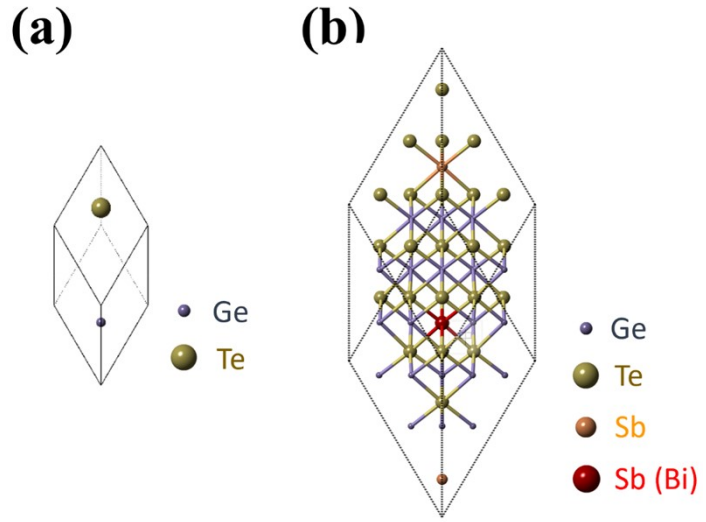

Figure S20 Crystal structure in the calculations for (a) undoped GeTe, and (b) Sb single-doped/Sb-Bi codoped GeTe ($Ge_{24}Sb_3Te_{27}$/$Ge_{24}Sb_2Bi_1Te_{27}$).

Figure S20 shows the crystal structures used for DFT calculations in this paper. It can be seen in Figure 5b that introducing Sb/Bi dopant of several percent does not cause qualitative change in the electronic structure except for slight wavevector/energy broadening. Thus, all the Fermi surface calculations in this paper used the crystal structure of undoped GeTe plotted in Fig. S20a with the Fermi level tuned to different positions for different hole concentrations.

Phonon dispersion

We calculate the phonon dispersion of undoped GeTe (2 atoms per unit cell) and Sb-Bi codoped GeTe (54 atoms per unit cell) with crystal structure shown in Figures S20a and S20b. The phonon dispersion was calculated by using PHONOPY code,[18] while for comparison purposes, that of the Sb-Bi codoped GeTe was also calculated by using the supercell phonon unfolding method implemented in the UPHO package.[19-21] The harmonic interatomic force constants (IFCs) required by the phonon calculations were calculated through DFT calculations in which the $6 \times 6 \times 6$ and $2 \times 2 \times 2$ supercells (both containing 432 atoms) are, respectively, considered, and $3 \times 3 \times 3$ and $2 \times 2 \times 2$ q-mesh are, respectively, used for undoped and doped GeTe.

Electron-phonon coupling

To complete the electron-phonon coupling simulations, Quantum Espresso package[22] with Ceperly-Alder (CA) type local density approximation (LDA)[23] and ultrasoft pseudopotential[24] are utilized. The **k**-grids 24×24×24 (12×12×12) and **q**-grids 4×4×4 are used for electron-phonon coupling (phonon bands) simulations. The electron-phonon coupling of point **q** can be expressed as:[25]

$$\lambda_{qv} \simeq \frac{1}{N_F \omega_{qv}} \sum_{mn,k} \left| g_{mn}^{v}(k,q) \right| \delta(\varepsilon_{nk} - \varepsilon_F) \delta(\varepsilon_{nk+q} - \varepsilon_F) \qquad \text{(eq 9)}$$

where $g_{mn}^{v}(k,q)$ the electron-phonon coefficients, N_F the electronic density of state (DOS) at the Fermi level ε_F per spin, and ω_{qv} (ε_{nk}) the energy of phonon (electronic) states.

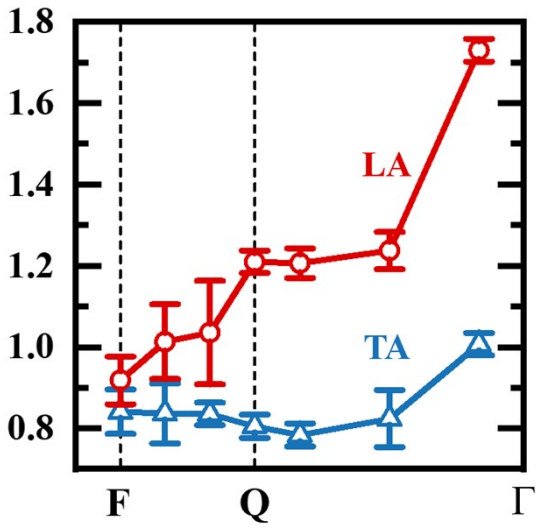

Figure S21 Variations of measured phonon lifetimes.

Phonon dispersion

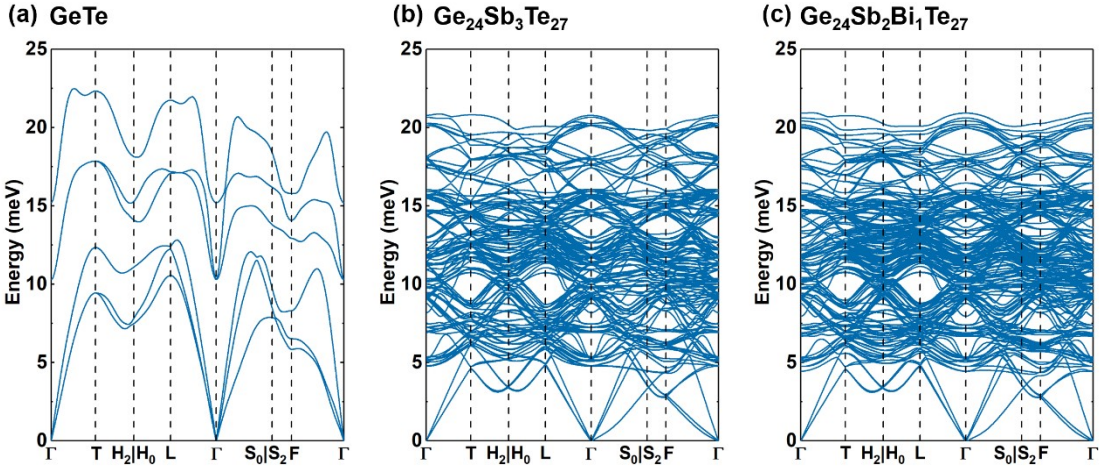

Figure S22 Phonon dispersion of (a) undoped GeTe unit cell (b) single Sb doped $Ge_{24}Sb_3Te_{27}$ supercell and (c) Sb-Bi codoped $Ge_{24}Sb_2Bi_1e_{27}$ supercell.

Figure S22 shows the phonon dispersion of pristine GeTe, single doped ($Ge_{24}Sb_3Te_{27}$), and codoped ($Ge_{24}Sb_2Bi_1Te_{27}$) structures. The unfolded phonon bands of the codoped ($Ge_{24}Sb_2Bi_1Te_{27}$) structure and density of modes (DOM) are shown in

Figures S23a and S23b for comparison with the pristine GeTe. As can be seen, for the pristine GeTe, there exists a continuous gap between the acoustic and optical phonon bands. The separated acoustic and optical modes significantly diminish the number of phonon-phonon scattering channels in pristine GeTe.[26] When the dopants are incorporated, regardless of single Sb doping or Sb-Bi codoping, the optical phonon modes are significantly softened, and some of them are reduced to the energy around the acoustic modes. This would significantly enhance the phonon-phonon scattering.

Contribution of Bi/Sb to phonon modes

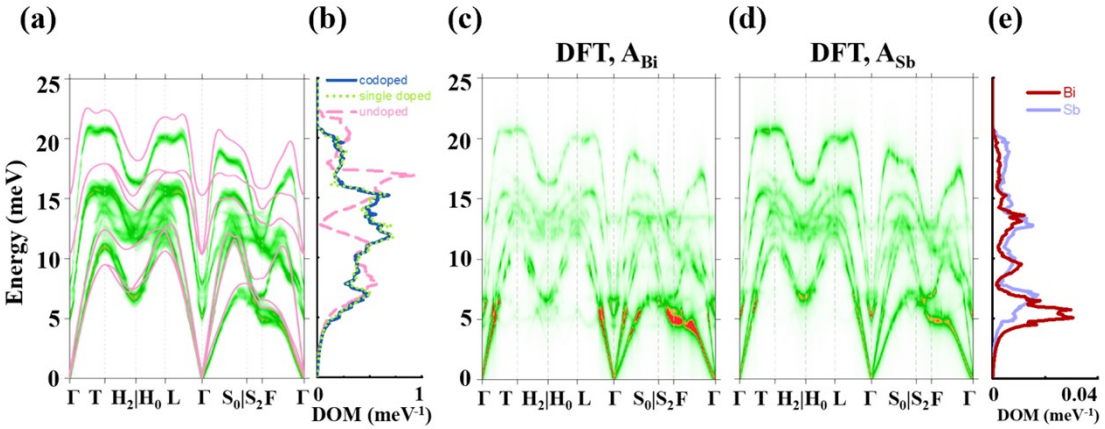

Figure S23 (a) Phonon dispersion of undoped GeTe structure shown in Figure S20a (pink bands) and that of Sb-Bi codoped structure (i.e., the $Ge_{24}Sb_2Bi_1Te_{27}$ in Figure S20b) unfolded to the Brillouin zone of undoped GeTe (green bands). (b) The corresponding density of modes as well as that of the Sb single doped structure ($Ge_{24}Sb_3Te_{27}$). (c,d) Projected phonon band structure of the Sb-Bi codoped GeTe unfolded onto the Brillouin zone of the undoped GeTe (Figure S22a) and (e) partial density modes. (c) and (d) are, respectively, projected onto Bi and Sb atoms.

Figures S23b-d shows the projected contribution from Bi and Sb to the calculated phonon band structures and phonon density of states of Sb-Bi codoped GeTe. It can be clearly seen that the Bi dopants contribute more to the low energy phonon

modes than Sb, especially to the lowest acoustic mode around F-point. Consequently, the codoped Bi dopants takes more part than Sb in the EP coupling mechanism to lower the lattice thermal conductivity of GeTe.

Calculation Methods

Details of single parabolic band modeling

Thermoelectric properties of single parabolic band model are given by Carrier concentration:[27]

$$n = \frac{\left(2m^* k_B T\right)^{3/2}}{2\pi^2 \hbar^3} F_{1/2}(\eta) \qquad \text{(eq 10)}$$

Seebeck coefficient:

$$S = \frac{k_B}{e}\left[\frac{2F_1(\eta)}{F_0(\eta)} - \eta\right] \qquad \text{(eq 11)}$$

Fermi integral:

$$F_x(\eta) = \int_0^\infty \frac{\varepsilon^x}{1 + exp(\varepsilon - \eta)} d\varepsilon \qquad \text{(eq 12)}$$

where m^* is the effective mass, $F_x(\eta)$ is the x-th order Fermi integral, and the Hall carrier density is related to the chemical carrier density n via $n_H = n/r_H$. r_H is the Hall factor for acoustic phonon scattering and is expressed as:

$$r_H = \frac{3F_{1/2}(\eta)\, F_{-1/2}(\eta)}{4 \quad F_0(\eta)^2} \qquad \text{(eq 13)}$$

The relationship between the Seebeck coefficient and Hall carrier density (Pisarenko relation) at 300 K and the suggested m_d^* are presented in Figure S24.

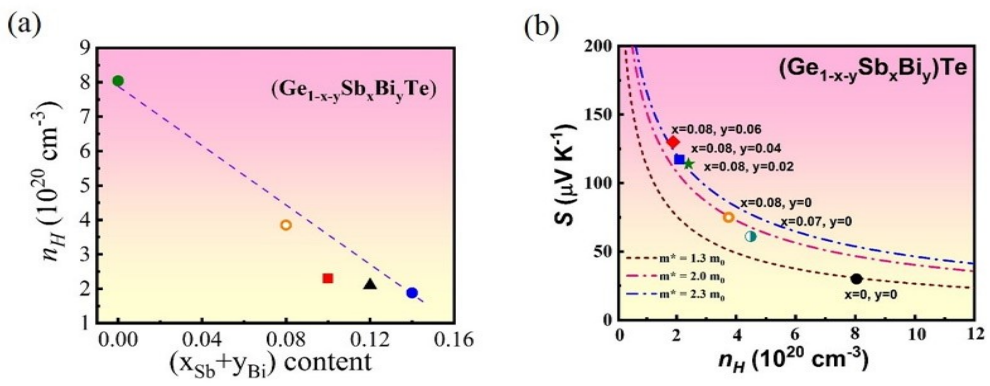

Figure S24 (a) Carrier concentration at different doping levels. (b) Theoretical Pisarenko plots are applied on experimental S vs n_H data of $(Ge_{1-x-y}Sb_xBi_y)Te$ at 300 K in which the m^* values were calculated by using a single parabolic band model.

Spin-orbit coupling effect

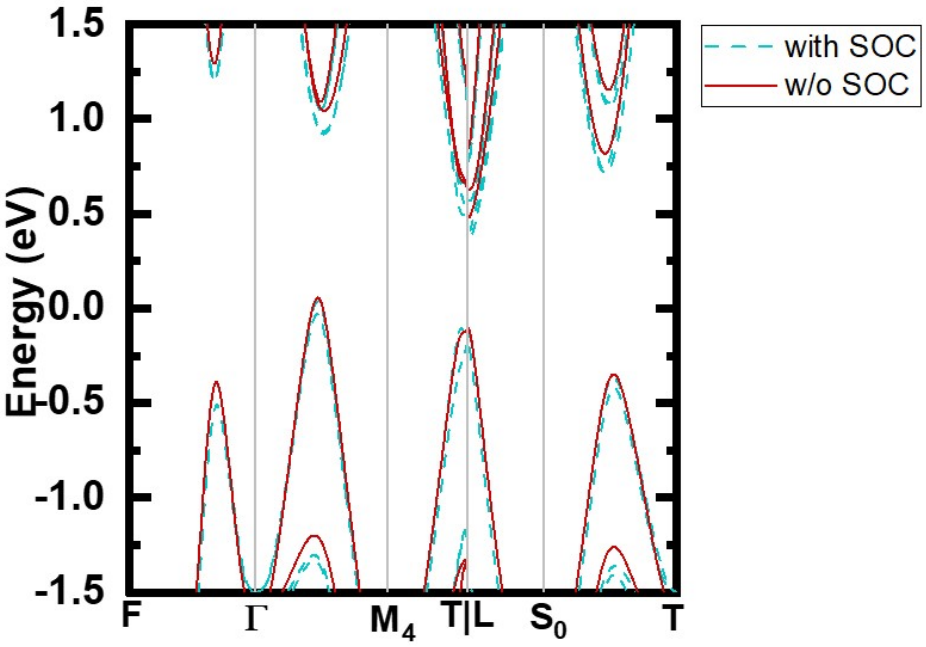

Figure S25 Electronic structure of GeTe with and without spin-orbit coupling

Figure S25 shows the electronic structure of GeTe with and without spin-orbit coupling. As can be seen, incorporating spin-orbit coupling would vary the electronic energy by few tens of milli-electronvolts. It would lead to quantitatively change in electronic transport properties but not qualitative change the low-dimensional features of the electronic structure and hence the mechanisms discussed in this paper.

Electron-phonon scattering processes causing a downturn in phonon dispersion

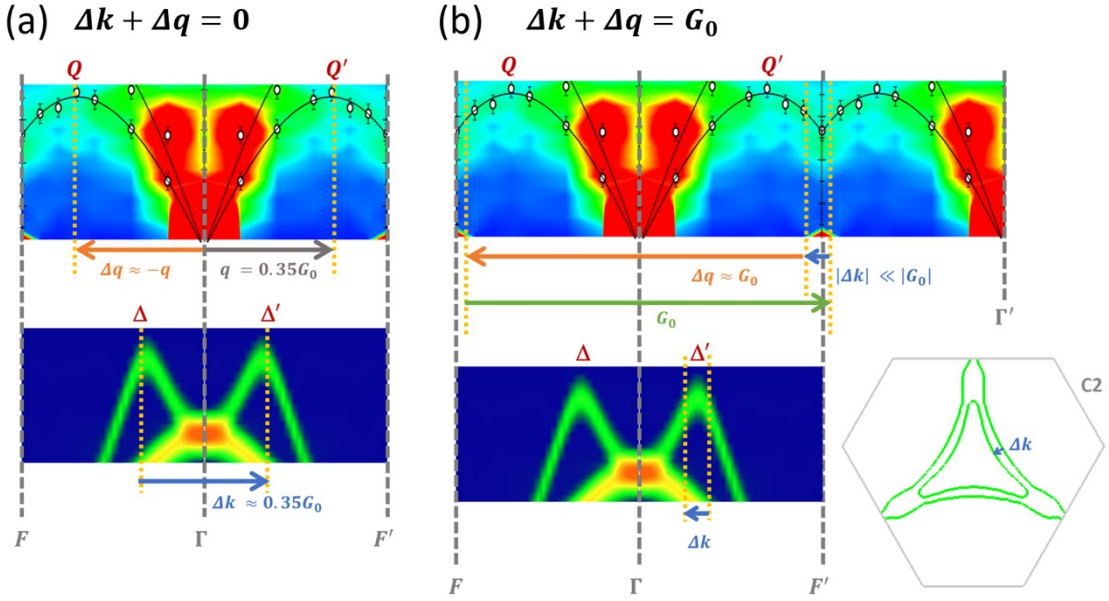

Figure S26 Illustration of the momentum conservation conditions, $\hbar\Delta k + \hbar\Delta q = \hbar G$, for (a) the first-order and (b) the second-order elastic electron-phonon scattering processes leading to the downturn of phonon dispersion. The $\hbar\Delta q$ ($\hbar\Delta k$) is the total change in the phonon (electron) crystal momentum due to the scattering process.

Figure S26 illustrates the electron-phonon scattering processes satisfying the momentum conservation condition, $\hbar\Delta k + \hbar\Delta q = \hbar G$. During the first-order scattering processes (Figure S26a), the change in the phonon crystal momentum $\hbar\Delta q$ is due to the single phonon creation (annihilation) of crystal momentum $-\hbar q$ ($\hbar q$). Figure S26b shows the second-order scattering process involving the intra-bowl electronic transition with a crystal momentum change $\hbar\Delta k$ much smaller than $\hbar G_0$. Here, G_0 is the smallest reciprocal lattice vector in [110] direction. In this process, the change in the phonon crystal momentum $\hbar\Delta q$ is either due to the two-phonon creation (annihilation) around the F ($F^{'}$) point or the one-phonon creation and the one-phonon annihilation, respectively, around F and $F^{'}$ points. Due to the nearly one-dimensional feature of the Fermi surface, enormous number of channels of the intra-bowl transitions has small

$\hbar\Delta k$ parallel to the [110] direction. This would lead to strong electron-phonon coupling strengthening the Kohn anomaly around the F point.

Here, we let the heat flow in the positive direction (i.e., $\Gamma \rightarrow F'$ direction) so that the phonon modes of positive crystal momentum (i.e., in between Γ and F') should be more populated than those of negative crystal momentum (i.e., in between Γ and F). Thus, the scattering processes tend to create (annihilate) phonon of negative (positive) crystal momentum restoring the thermal equilibrium. The counterparts of scattering processes of reversing $\hbar\Delta q$ is less important and thus not plotted in Figure S26. It is worth noting that the second-order processes are essentially the same as the three-phonon Umklapp process except that the role of one of the phonons is replaced by the electronic transition. Both the first-order and the second-order processes would reduce the thermal conductivity as indicated by their negative direction of $\hbar\Delta q$, the direction opposite to the presumed direction of heat flow.

Wave functions of 1D-like electronic state

To reveal the origin of the 1D-like Fermi surface, we plot the wave function of the Δ maximum as shown in Figures S27b-d. There are six equivalent Δ points within the first Brillouin zone. Here, as an example, we choose the Δ point along the ΓX as denoted by the green cross in Figure S27d. The phase of the wave function is selected to maximize the probability contribution of the real part of the wave function to the value of 0.79. As shown in Figures S27b-c, the real part of the wave function at the Δ point along ΓX is p_x-like while the imaginary part is s-like localized around the Ge atoms leading to the wave function of the shape like parallel chains oriented in the x direction. It exhibits strong orbital overlap along the x direction (i.e., intra-chain overlap) but weak overlap in the y and z directions (i.e., inter-chain overlap). As a result, the

electronic structure around the Δ point along ΓX is nearly flat in the y and z directions while it is much more dispersive in the x direction forming the double-walled Fermi surface with the normal along the x direction (Figure S27e). Because of the cubic symmetry, similar results can be found for the Δ points along ΓY and ΓZ as indicated by Figure S27d. These chain-like wave functions around the Δ points effectively act as dense nanowires in bulk leading to the observed ultrahigh thermoelectric performance in GeTe-based materials.

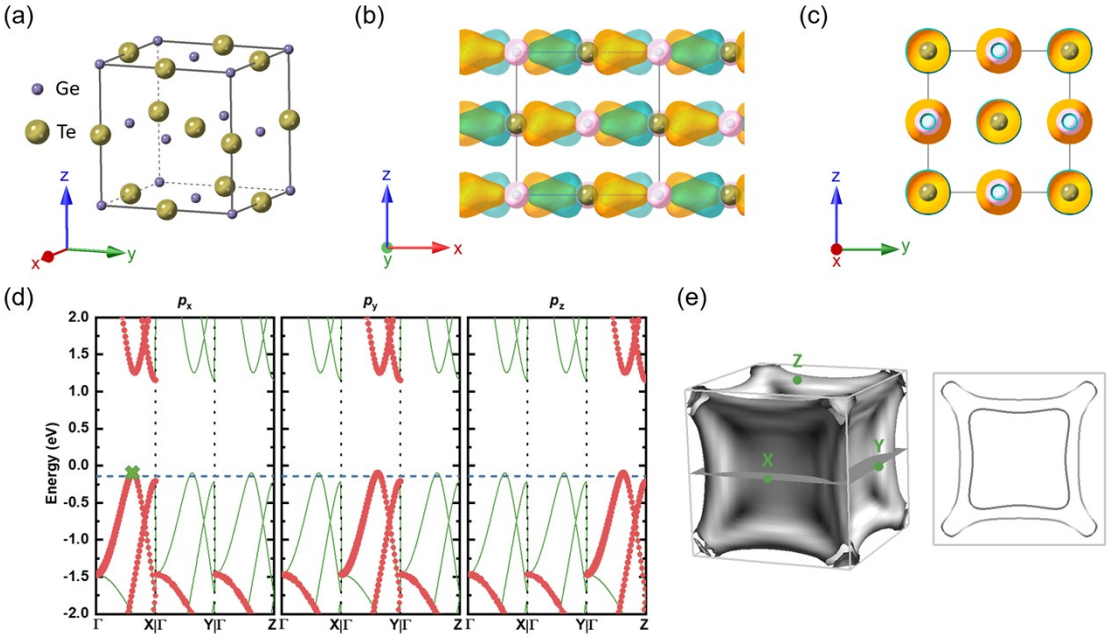

Figure S27 One-dimensional electronic states in bulk GeTe. (a) The conventional cell of C-GeTe. (b, c) The isosurface of the wave function at the Δ maximum along ΓX as denoted by the green cross in (d). The orange/green surfaces are for the real part of the wave function with positive/negative sign while the pink one is for the imaginary part with positive sign. All the isosurfaces are set at the same magnitude. The magnitude for the imaginary part of negative sign is too small so that the corresponding isosurface do not exist. (d) The electronic structure plotted in the Brillouin zone shown in (e) of the conventional cell in (a). The weight of the p_x, p_y and p_z orbitals are indicated by the size of the red dots, respectively, in the left, middle, and right panels. (e) The Fermi surface and the corresponding cross-section with the Fermi energy denoted by the dashed line in (d).

Cost and stability issues in GeTe-based materials

1. Cost:

Whether thermoelectric power generation technology can be widely used depends not only on performance, but also on the cost-performance ratio.[28,29] Taking photovoltaic (PV) cells as an example, its cost-performance ratio of ~1 dollar per watt ($/watt) makes them competitive in the market. Similarly, we also use such evaluation way to analyze whether the Sb-Bi codoped GeTe materials have the same energy competition. Here, we refer to a guiding approach developed by Quyang *et al*,[30] namely the cost-performance ratio, for the TEG generation. According to their analytical results, a high-zT thermoelectric material with 17.8 % efficiency and a power density exceeding 3.0 W/cm^2 has the opportunity to achieve a cost-performance ratio of ~0.86 $/W. The most important thing is that the zT value will have a significant impact on the ratio. According to our estimation results, ($Ge_{0.86}Sb_{0.08}Bi_{0.06}$)Te also has an efficiency of 17.4 % and a zT value much higher than that used in the above analytical model. Although the element price of Ge is relatively high, after weighing various factors such as: the capital cost of the device and power generation, its cost performance ratio should not be much higher than ~1 $/W. Therefore, we believe that Sb-Bi codoped GeTe materials still have extremely high application potential compared with existing typical high-efficiency thermoelectric materials.

2. Mechanical properties:

Generally, the indicator to evaluate whether a material can withstand long-term working operation is to measure its mechanical properties through Vickers hardness measurement. According to literature data,[3] the Vickers hardness measurements of GeTe-based thermoelectric materials (145~205 Hv) are much higher than those typical Bi-Te-based and Pb-Te-based thermoelectric materials. Especially, the introduction of

dopants such as Sb, Bi, and Pb has been confirmed to achieve the reduced Ge vacancies and the enhanced solid solution and rich microstructures, thereby blocking the crack propagation and enhancing the mechanical stability. Our research is to co-dope GeTe with Sb and Bi, and we also observed that the Ge vacancies are significantly reduced, so we believe that our samples also have such excellent mechanical properties.

3. Thermal stability:

We took the $Ge_{0.86}Sb_{0.08}Bi_{0.06}Te$ sample as a representative to measure the thermoelectric properties of the heating-cooling twice to understand the thermal stability of the sample, as shown in Figure S28. The transport properties and the narrow statistical distribution of zT values measured from the sample confirm the superior thermal stability of the sample.

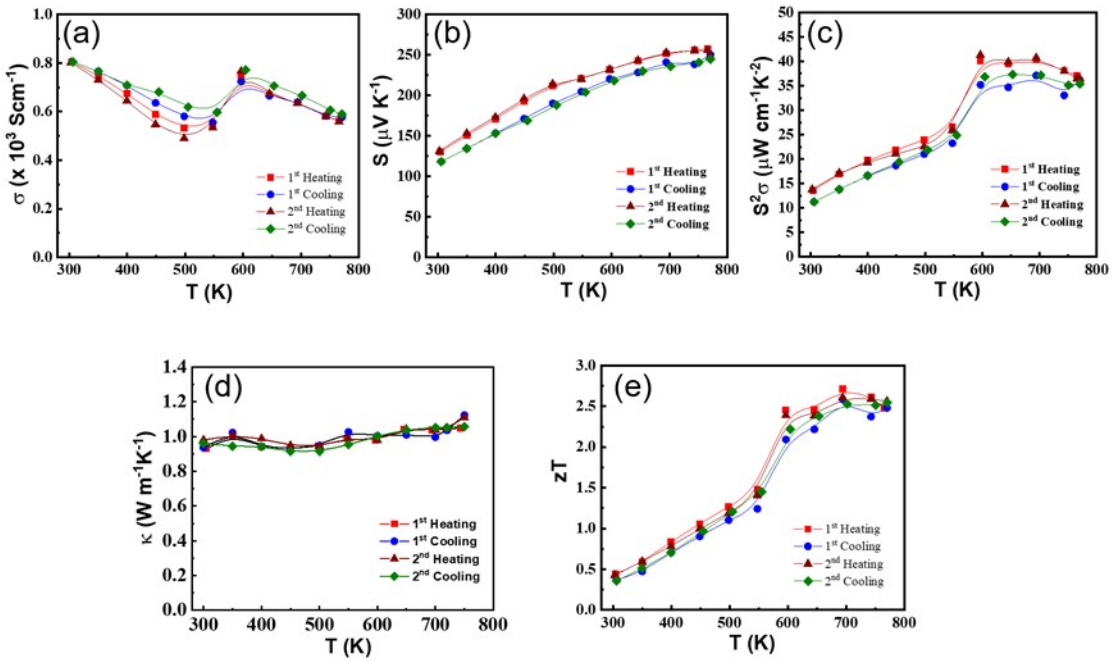

Figure S28 The heating and cooling measurements for $Ge_{0.86}Sb_{0.08}Bi_{0.06}Te$ sample, showing good thermal stability for a high zT value in this work. (a) Electrical conductivity. (b) Seebeck coefficient. (c) Power factor. (d) Thermal conductivity. (e) zT value.

Mobility of undoped and Sb-Bi codoped specimens

The mobility of our specimens can be evaluated by $\mu = \sigma/en$, in which n is the carrier concentration obtained through Hall measurement, σ the electrical conductivity (Figure. 2a), and e the elementary charge. The resulting mobility is shown in Figure S29. It may be worth noting that the mobility shown in Figure S29 is based on the room-temperature carrier concentration, which may slightly increase with increasing temperature, potentially resulting in a slight underestimation of mobility. As can be seen, the room-temperature mobility of undoped GeTe is 68.6 $cm^2\ V^{-1}s^{-1}$ and that of $Ge_{0.86}Sb_{0.08}Bi_{0.06}Te$, which is the specimen of highest zT, is as low as 26.7 $cm^2\ V^{-1}s^{-1}$. These values are much smaller than most semiconductors such as Si (1400 $cm^2\ V^{-1}s^{-1}$), Ge (3900 $cm^2\ V^{-1}s^{-1}$) and GaAs (8500 $cm^2\ V^{-1}s^{-1}$), probably mainly due to the strong electron-phonon coupling caused by the nesting Femi surface. Although the mobility is quite low, the high effective valley degeneracy resulting from 1D/2D-like electronic structure will mitigate the deterioration of the Seebeck coefficient caused by high carrier concentration, and hence lead to the observed large power factor in our specimens.

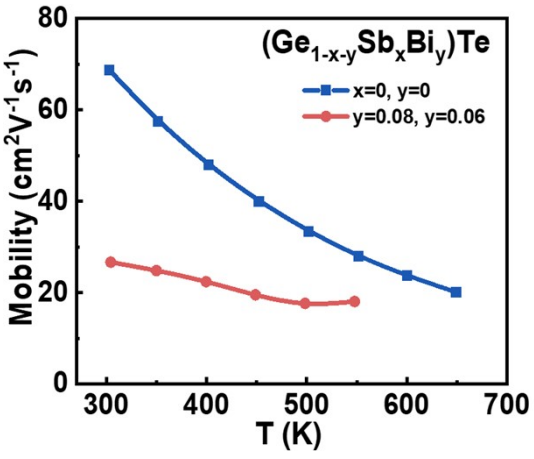

Figure S29 Mobility of undoped and Sb-Bi codoped specimens.

References

1 X. Xu, L. Xie, Q. Lou, D. Wu, J. He, Boosting the thermoelectric performance of pseudo-layered $Sb_2Te_3(GeTe)_n$ via vacancy engineering. *Adv. Sci.* 2018, **5**, 1801514.

2 X. Zhang, Z. Bu, S. Lin, Z. Chen, W. Li, Y. Pei, GeTe thermoelectrics. Joule, 2020, **4**, 986-1003.

3 M. Hong, K. Zheng, W. Lyv, M. Li, X. Qu, Q. Sun, S. Xu, J. Zou, Z. G. Chen, Computer-aided design of high-efficiency GeTe-based thermoelectric devices, *Energy Environ. Sci.* 2020, **13**,1856-1864.

4 G. Kresse, J. Furthmuller, Efficiency of Ab-Initio total energy calculations for metals and semiconductors using a plane-wave basis set. *Comput. Mater. Sci.* 1996, **6**, 15-50.

5 G. Kresse, Ab-Initio molecular-dynamics for liquid-metals. *J. Non-Cryst. Solids,* 1995, **193**, 222-229.

6 G. Kresse, J. Furthmuller, Efficient iterative schemes for Ab Initio total-energy calculations using a plane-wave basis set. *Phys. Rev. B,* 1996, **54**, 11169-11186.

7 J. P. Perdew, J. A. Chevary, S. H. Vosko, K. A. Jackson, M. R. Pederson, D. J. Singh, C. Fiolhais, Atoms, molecules, solids, and surfaces: applications of the generalized gradient approximation for exchange and correlation. *Phys. Rev. B,* 1992, **46**, 6671-6687.

8 J. P. Perdew, Y. Wang, Pair-distribution function and its coupling-constant average for the spin-polarized electron-gas. *Phys. Rev. B,* 1992, **46**, 12947-12954.

9 A. J. Cohen, P. Mori-Sanchez, W. T. Yang, Insilghts into current limitations of density functional theory. *Science,* 2008, **321**, 792-794.

10 R. Tsu, W. E. Howard, L. Esaki, Optical and electrical properties and band structure of GeTe and SnTe. *Phys. Rev.* 1968, **172**, 779-788.

11 T. -H. Wang, H. -T. Jeng, Topological insulator nanoribbons – a new paradigm for high thermoelectricperformance. *Nano Energy,* 2019, **66**, 104092.

12 T. -H. Wang, H. -T. Jeng, Strongly enhanced thermoelectric performance over a wide temperature range in topological insulator thin films. *ACS Appl. Energy*

Mater. 2018, **1**, 5646-5655.

13 M. Lundstrom, *Fundamentals of carrier transport*. (Cambridge University Press, 2009).

14 J. Callaway, Model for Lattice thermal conductivity at low temperatures, *Phys. Rev.* 1959, **113**, 1046-1051.

15 R. K. Vankayala, T. W. Lan, P. Parajuli, F. Liu, R. Rao,S. H. Yu, T. L. Hung, C. H. Lee, S. Yano, C. R. Hsing, D. L. Nguyen, C. L. Chen, S. Bhattacharya, K. H. Chen, M. N. Ou, O. Rancu, A. M. Rao, Y. Y. Chen, High zT and Its origin in Sb-doped GeTe single crystals, *Adv. Sci.* 2020, **7**, 2002494.

16 Y. Gelbstein, J. Davidow, E. Leshem, O. Pinshow, S. Moisa, Significant lattice thermal conductivity reduction following phase separation of the highly efficient $Ge_xPb_{1-x}Te$ thermoelectric alloys, *Phy. Status Solidi (b),* 2014, **251**, 1431-1437.

17 T. Fang, J. Xin, C. Fu, D. Li, X. Zhao, C. Felser, T. Zhu, Influence of electron–phonon interaction on the lattice thermal conductivity in single-crystal Si, *Ann. Phys.*(*Berlin*) 2020, **532**, 1900435.

18 A. Togo, I. Tanaka, First principles phonon calculations in materials science. *Scripta Mater,* 2015, **108**, 1-5.

19 T. B. Boykin, N. Kharche, G. Klimeck, M. Korkusinski, Approximate bandstructures of semiconductor alloys from tight-binding supercell calculations. *J. Phys.: Condens. Matter,* 2007, **19,** 036203.

20 P. B. Allen, T. Berlijn, D. A. Casavant, J. M. Soler, Recovering hidden bloch character: unfolding electrons, phonons, and slabs. *Phys. Rev. B,* 2013, **87**, 085322.

21 Y. Ikeda, A. Carreras, A. Seko, A. Togo, I. Tanaka, Mode decomposition based on crystallographic symmetry in the band-unfolding method. *Phys. Rev. B,* 2017, **95**, 024305.

22 P. Giannozzi, O. Andreussi, T. Brumme, O. Bunau, M. B. Nardelli, M. Calandra, R. Car, C. Cavazzoni, D. Ceresoli, M. Cococcioni, N. Colonna, I. Carnimeo, A. Dal Corso, S. de Gironcoli, P. Delugas, R. A. DiStasio Jr., A. Ferretti, A. Floris, G. Fratesi, G. Fugallo, R. Gebauer, U. Gerstmann, F. Giustino, T. Gorni, J. Jia, M. Kawamura, H. -Y. Ko, A. Kokalj, E. Kucukbenli, M. Lazzeri, M. Marsili, N. Marzari, F. Mauri, N. L. Nguyen, H. -V. Nguyen, A. Otero-de-la-Roza, L. Paulatto, S. Ponc´e, D. Rocca, R. Sabatin, B. Santra, M. Schlipf, A. P. Seitsonen, A. Smogunov, I. Timrovi, T. Thonhauser, P. Umariu, N. Vast, X. Wu, S. Baroni, Advanced capabilities for materials modelling with quantum espresso. *J. Phys.: Condens. Matter,* 2017, **29**, 465901.

23 D. M. Ceperley, B. J. Alder, Ground state of the electron gas by a stochastic

method. *Phys. Rev. Lett.* 1980, **45**, 566-569.

24 D. Vanderbilt, Soft self-consistent pseudopotentials in a generalized eigenvalue formalism. *Phys. Rev. B,* 1990, **41**, 7892-7895.

25 R. Heid, in Emergent phenomena in correlated matter modeling and simulation Vol. **3** (eds E. Pavarini, E. Koch, & Ulrich Schollwöck) (2013).

26 M. Hong, Y. Wang, T. Feng, Q. Sun, S. Xu, S. Matsumura, S. T. Pantelides, J. Zou, Z. G. Chen, Strong phonon-phonon interactions securing extraordinary thermoelectric $Ge_{1-x}Sb_xTe$ with Zn-alloying-induced band alignment. *J. Am. Chem. Soc.* 2019, **141**, 1742-1748.

27 Y. Pei, A. D. LaLonde, H. Wang, G. J. Snyder, Low effective mass leading to high thermoelectric performance. *Energy Environ. Sci.* 2012, **5**, 7963-7969.

28 S. LeBlanc, S. K. Yee, M. L. Scullin, C. Dames, K. E. Goodson, Material and manufacturing cost considerations for thermoelectrics. *Renew. Sustain. Energy Rev*. 2014, **32**, 313-327.

29 S. K. Yee, S. LeBlanc, K. E. Goodson, C. Dames, $ per W metrics for thermoelectric power generation: beyond ZT. *Energy Environ. Sci.* 2013, **6,** 2561-2571.

30 Z. Ouyang, D. Li, Design of segmented high-performance thermoelectric generators with cost in consideration. *Appl. Energy*, 2018, **221**, 112-121.